the plant journal

SEB Society for Experimental Biology

The Plant Journal (2017) **91,** 340–354 doi: 10.1111/tpj.13569

TECHNICAL ADVANCE

Laser-ablation electrospray ionization mass spectrometry with ion mobility separation reveals metabolites in the symbiotic interactions of soybean roots and rhizobia

Sylwia A. Stopka[1], Beverly J. Agtuca[2], David W. Koppenaal[3], Ljiljana Paša-Tolić[3], Gary Stacey[2], Akos Vertes[1] and Christopher R. Anderton[3,*]

[1]*Department of Chemistry, W. M. Keck Institute for Proteomics Technology and Applications, The George Washington University, Washington, DC 20052, USA,*

[2]*Divisions of Plant Sciences and Biochemistry, C. S. Bond Life Sciences Center, University of Missouri, Columbia, MO 65211, USA, and*

[3]*Environmental Molecular Sciences Laboratory, Earth and Biological Sciences Directorate, Pacific Northwest National Laboratory, 902 Battelle Boulevard, Richland, WA 99354, USA*

Received 14 February 2017; revised 3 April 2017; accepted 4 April 2017; published online 10 April 2017.
*For correspondence (e-mail christopher.anderton@pnnl.gov).

SUMMARY

Technologies enabling *in situ* metabolic profiling of living plant systems are invaluable for understanding physiological processes and could be used for rapid phenotypic screening (e.g., to produce plants with superior biological nitrogen-fixing ability). The symbiotic interaction between legumes and nitrogen-fixing soil bacteria results in a specialized plant organ (i.e., root nodule) where the exchange of nutrients between host and endosymbiont occurs. Laser-ablation electrospray ionization mass spectrometry (LAESI-MS) is a method that can be performed under ambient conditions requiring minimal sample preparation. Here, we employed LAESI-MS to explore the well characterized symbiosis between soybean (*Glycine max* L. Merr.) and its compatible symbiont, *Bradyrhizobium japonicum*. The utilization of ion mobility separation (IMS) improved the molecular coverage, selectivity, and identification of the detected biomolecules. Specifically, incorporation of IMS resulted in an increase of 153 differentially abundant spectral features in the nodule samples. The data presented demonstrate the advantages of using LAESI–IMS–MS for the rapid analysis of intact root nodules, uninfected root segments, and free-living rhizobia. Untargeted pathway analysis revealed several metabolic processes within the nodule (e.g., zeatin, riboflavin, and purine synthesis). Compounds specific to the uninfected root and bacteria were also detected. Lastly, we performed depth profiling of intact nodules to reveal the location of metabolites to the cortex and inside the infected region, and lateral profiling of sectioned nodules confirmed these molecular distributions. Our results established the feasibility of LAESI–IMS–MS for the analysis and spatial mapping of plant tissues, with its specific demonstration to improve our understanding of the soybean-rhizobial symbiosis.

Keywords: nitrogen fixation, root nodules, LAESI, ion mobility separation, metabolites, *Glycine max*, *Bradyrhizobium japonicum*, technical advance.

INTRODUCTION

In order to address global issues concerning agriculture, biofuel production, and environmental sustainability, new technologies and approaches are being developed for comprehensively analyzing the complex biochemical

networks within plant systems (Gemperline *et al.*, 2016). Specifically, the "omics cascade" approach of systems biology investigates the global changes within the genes, proteins, and metabolites of an organism (Dettmer *et al.*, 2007; Pu and Brady, 2010). Significant advancements and breakthroughs have been established in genomics, transcriptomics, and proteomics, whereas technologies to monitor the downstream effects (e.g., metabolomics) are slowly emerging (Weckwerth, 2003; Gemperline *et al.*, 2016) The majority of metabolomic methods require extensive sample preparation and cannot be performed *in situ*. Nevertheless, these approaches have predicted over 200 000 metabolites within the plant kingdom, consisting of species-independent compounds of primary and secondary small molecules (Fiehn, 2002; Dixon and Strack, 2003). To date, technologies have been developed for metabolite profiling for a variety of well-characterized plant systems that include, but are not limited to, tomato (Schauer *et al.*, 2006; Oms-Oliu *et al.*, 2011), *Arabidopsis* (Fiehn, 2006; Schmidt *et al.*, 2014), *Medicago truncatula* (Schliemann *et al.*, 2008; Zhang *et al.*, 2014), and *Glycine max* (Benkeblia *et al.*, 2007).

Technologies that can metabolically profile plant systems *in situ* provide a clearer understanding of processes like growth and development, which are heavily influenced by the accessibility of nitrogen within the surrounding environment (Crawford, 1995). Addressing these challenges can reduce our dependence on nitrogen-based fertilizers for maintaining nutrient availability to improve crop yields (Sulieman, 2011). Moreover, current practices lead to excess nitrogen not consumed by the crops, which can end up as chemical runoff, contaminating nearby water supplies (Zahran, 1999). Exploring and understanding certain plant and microbial systems that are known to obtain nitrogen through biological nitrogen fixation (BNF), such as sugarcane (Oliveira *et al.*, 2002), specific legumes (Freiberg *et al.*, 1997), and blue-green algae (Allen and Arnon, 1955) can result in more sustainable agricultural practices.

In particular, legumes possess the unique ability to develop symbiotic interactions with nitrogen-fixing soil bacteria (i.e., rhizobia). This mutualism manifests in the formation of specialized plant organs referred to as root nodules (Vanrhijn and Vanderleyden, 1995). Within these specialized organs, BNF occurs, where the endosymbiont transforms atmospheric nitrogen into ammonia for the host, and in return carbon is supplied in the form of photosynthates to the rhizobia (Stacey, 2007; White *et al.*, 2007). Well established proteomic and transcriptomic analyzes have demonstrated important conclusions in regards to the nodules and the effects of environmental perturbations. Over 800 genes have been identified to be highly expressed in the nodules. Among these were approximately 80 nodule-induced genes that were involved in sugar and amino acid metabolism (Colebatch *et al.*, 2004). Within the single-cell model system of soybean root hairs infected by *Bradyrhizobium japonicum*, a total of approximately 1973 identified genes were differentially expressed during the host-rhizobia symbiotic interaction (Libault *et al.*, 2010). A tremendous amount of genomic information has been gathered about these legume-rhizobia symbioses. However, in comparison, relatively little is known about the biochemical transformations, metabolite composition, and the downstream effects occurring within nodules (Stacey *et al.*, 2006).

Detection of plant metabolites is extremely challenging as there is no single technique for their total coverage. Mass spectrometry (MS)-based approaches are most commonly utilized in metabolomics (Fiehn *et al.*, 2000). These methods can provide invaluable insights into the metabolic cascades of plant–bacterial interactions because of their ability to measure multiple biomolecules simultaneously (van der Drift *et al.*, 1998). Plant extracts and exudates have been investigated using gas chromatography-MS (GC-MS) (Barsch *et al.*, 2006), high performance liquid chromatography-MS (LC-MS) (Wang *et al.*, 2015), and capillary electrophoresis–MS (Harada and Fukusaki, 2009), which are highly sensitive methods and can provide quantitative information. However, these bulk analysis methods require extensive sample preparation, have low-throughput, and do not retain information on the spatial distribution of metabolites within plant tissues or organs. Other techniques can elucidate spatial distributions of metabolites *in situ* (e.g., matrix assisted laser desorption/ionization), but often require a vacuum environment and other perturbations to the sample (Ye *et al.*, 2013; Boughton *et al.*, 2015; Gemperline *et al.*, 2015).

Ambient ionization MS-based platforms, like laser-ablation electrospray ionization (LAESI) and desorption electrospray ionization (DESI), require minimal sample preparation and can provide measurements for biological samples in their native conditions (Nemes and Vertes, 2007; Mueller *et al.*, 2011). In particular, LAESI-MS has been a growing technique in the field of plant metabolomics. LAESI-MS utilizes a mid-IR laser tuned to the strongest water absorption band, making it ideal for ablating water-rich plant samples. As a result, this technology can be used to investigate intact biological samples in a high-throughput fashion. A limiting factor for this technology is not distinguishing isobaric species, which can be mitigated by employing a separation step (Etalo *et al.*, 2015).

In recent years, ion mobility separation (IMS), a conceptually orthogonal technique, has been combined with MS to enable enhanced distinction of ionic species in the analysis of complex biological samples. A wide range of bio-related applications has been reported using IMS–MS platforms, which include structural characterization of carbohydrates, determining the positions of fatty acyl chains and double bonds in lipids, imaging structural isomers in

biological tissues, and signal enhancement of low concentration biomolecules (Borsdorf and Eiceman, 2006; Castro-Perez *et al.*, 2011; Li *et al.*, 2012, 2015; Gaye *et al.*, 2015). Separation of ions by IMS is based on the differences in their collision cross-section (CCS) amplitudes, which is reflected in different drift time (DT) values measured while being driven through a carrier gas by an electric field (Kanu *et al.*, 2008; Shvartsburg and Smith, 2008; Wyttenbach *et al.*, 2014). The time scale of separation in IMS is on the order of milliseconds, which compares favorably with the multiple minutes required in liquid chromatography (LC), and allows for integration into high-throughput untargeted workflows (Paglia *et al.*, 2014; May *et al.*, 2015). Recently, LAESI-MS has been coupled with IMS, where it produced a significant increase in the molecular coverage of detected metabolites (Shrestha and Vertes, 2014). It also aided with the elucidation of lipid species by allowing for time-aligned parallel fragmentation directly from native plant and microorganism samples (Stopka *et al.*, 2014, 2016).

Here, we demonstrate the utility of LAESI–IMS–MS to directly analyze free-living rhizobia, soybean roots, and root nodules. We also demonstrate a 'proof of concept' for depth profiling intact nodules by controlled ablation through the cortex and into the infected region to determine the spatial distributions of metabolites throughout the anatomical regions. Comparing these results to LAESI–IMS–MS analysis of free-living bacteria and uninfected root segments, we were able to correlate spectral features with the nodule anatomy, and to elucidate the generation of symbiotically induced metabolites. This approach can translate into the rapid screening of BNF mutants and other biological systems. Further, these results demonstrate the feasibility of LAESI–IMS–MS for untargeted metabolite profiling in plant research.

RESULTS

To establish the applicability of LAESI–IMS–MS for plant metabolite profiling analysis, the well characterized symbiosis between soybean [*Glycine max* (L.) Merr.] and its compatible symbiont, *B. japonicum*, was selected because of the extensive genetic knowledge of both of these systems. Here, we demonstrated two different analysis approaches for the rapid profiling of metabolites. First, free-living rhizobial cell pellets and bulk material from homogenized root nodules and uninfected roots were analyzed to obtain the metabolite coverage of rhizobia and each plant system. Univariate, multivariate, and hierarchical clustering statistical analysis methods were applied to these data in the form of volcano plots, partial least squares discriminant analysis (PLS-DA), and heat maps, respectively. The second approach involved depth profiling of intact nodules to maintain spatial information of metabolite abundance throughout the different anatomical layers. This analysis involved controlling the laser pulses as a function of time.

The ambient nature and high-throughput capability of LAESI–IMS–MS made it an ideal method for exploring the plant–rhizobia symbiotic relationship. The incorporation of IMS provided an additional dimension of separation without sacrificing the rapid analysis of biological liquids, as well as tissue samples in their native states. Briefly, the working principles of LAESI–IMS–MS analysis involved tuning a mid-IR laser to the resonant frequency of the O–H vibrations of water at 2.94 μm. To facilitate laser induced material ablation from plant tissue, focused nanosecond

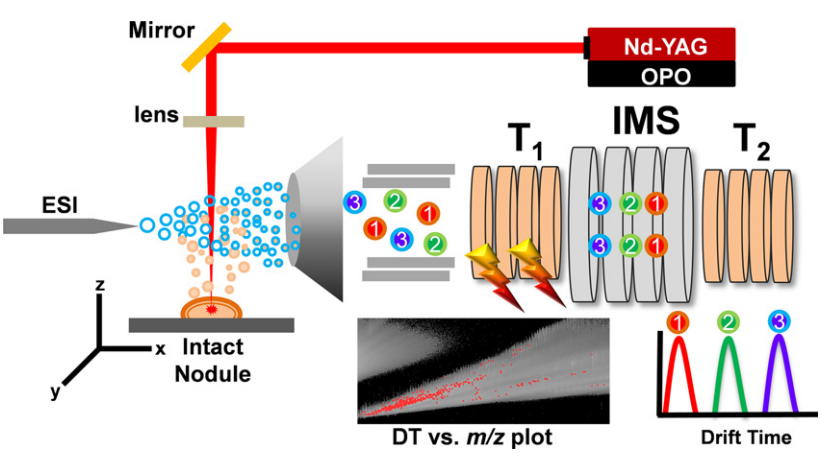

Figure 1. Schematic of LAESI–IMS–MS analysis.
A mid-IR laser delivered nanosecond pulses directly into an intact nodule or biological sample. The produced ablation plume was intercepted by an orthogonal ESI spray, which resulted in the production of ions. The ions were then sampled by the mass spectrometer and ion mobility separation was employed for the enhancement of molecular coverage. Specifically, within the mass spectrometer, ions were first selected by a quadrupole based on their *m/z*, including isobaric species indicated as species 1 to 3. A tri-wave-based ion mobility system allowed the ions to pass through the trap cell (T_1) into the IMS cell. Here, using N_2 as the drift gas, an induced electric field drove and separated the isobaric ions based on their physical structure into the transfer cell (T_2). Within T_1, collision induced dissociation was used to elucidate structural information for tandem MS.

laser pulses where directed into the water-rich samples, producing an ablation plume of neutrals (Figure 1). The expanded plume was then captured and ionized by an electrospray in-axis with the mass spectrometer orifice, in which ions were sampled in both positive and negative ion modes. To extend the molecular coverage, IMS was integrated into the LAESI workflow. This provided the ability to separate isobaric species. The use of CCS values provided further confidence in metabolite identifications.

Metabolite coverage of biological systems by LAESI–MS

The rapid metabolite profiling by LAESI–MS was performed on free-living rhizobia, along with homogenized nodules and uninfected root segments (Figure 2). The corresponding mass spectra were processed using the open MS tool mMass software (Strohalm *et al.*, 2008) by the removal of naturally abundant isotope peaks (so-called 'deisotoping'). In order to determine the number of unique spectral features, we also excluded redundant peaks attributed to sodium and potassium adducts of accounted-for $[M+H]^+$ quasi-molecular ions. After post-processing, a representative mass spectrum from free-living *B. japonicum* revealed about 456 spectral features, of which 208 and 248 features were detected in negative and positive ion modes, respectively (Figure 2a,d). A typical uninfected root sample had a metabolite coverage of approximately 461 spectral features, where 266 and 143 features were detected in negative and positive ion modes, respectively (Figure 2b,e). Lastly, the nodule samples exhibited the largest molecular coverage of approximately 797, where negative ion mode revealed 536 features, while positive ion mode contained 304 features (Figure 2c,f).

Several molecules were tentatively assigned to and correlated with specific sample groups (Table S1). For example, energy-related species, such as $[AMP\text{-}H]^-$, $[ADP\text{-}H]^-$, and $[ATP\text{-}H]^-$, at *m/z* 346.064, 426.026, and 505.991, respectively, were observed in the free-living rhizobia. However, sugars, glucosides, flavonones, and triterpenes (e.g., [trihydroxyflavone glucoside-H]$^-$ at *m/z* 431.095, [dihydroxyflavone+H]$^+$ at *m/z* 255.063, and [soyasaponin βg+H]$^+$ at m/z 1069.551) were present at high abundance in both uninfected plant tissue and root nodules. Uninfected plant tissue molecules were also ascertained. For example, molecular species detected only in the uninfected root included [trihydroxy trimethoxyflavone glucuronide-H]$^-$ at *m/z* 535.107. Molecules specific to the nodule samples included an abundance of [heme *B*]$^+$ at *m/z* 616.179 and low amounts of [oleic acid-H]$^-$at *m/z* 281.248. These results are in good agreement with previous studies that show a significant presence of heme (Nadler and Avissar, 1977) and oleic acid-based lipids (Gaude *et al.*, 2004) in soybean nodules. Molecular species detected in all three sample types included nucleotides (e.g., [guanine+H]$^+$ at *m/z* 152.052 and [adenosine+H]$^+$ at *m/z* 268.104), [disaccharide+Na]$^+$ at *m/z* 365.106, and several other ions.

LAESI-MS is well established as a soft ionization method for facilitating the characterization of intact molecules, including intact proteins (Kiss *et al.*, 2014), in contrast to

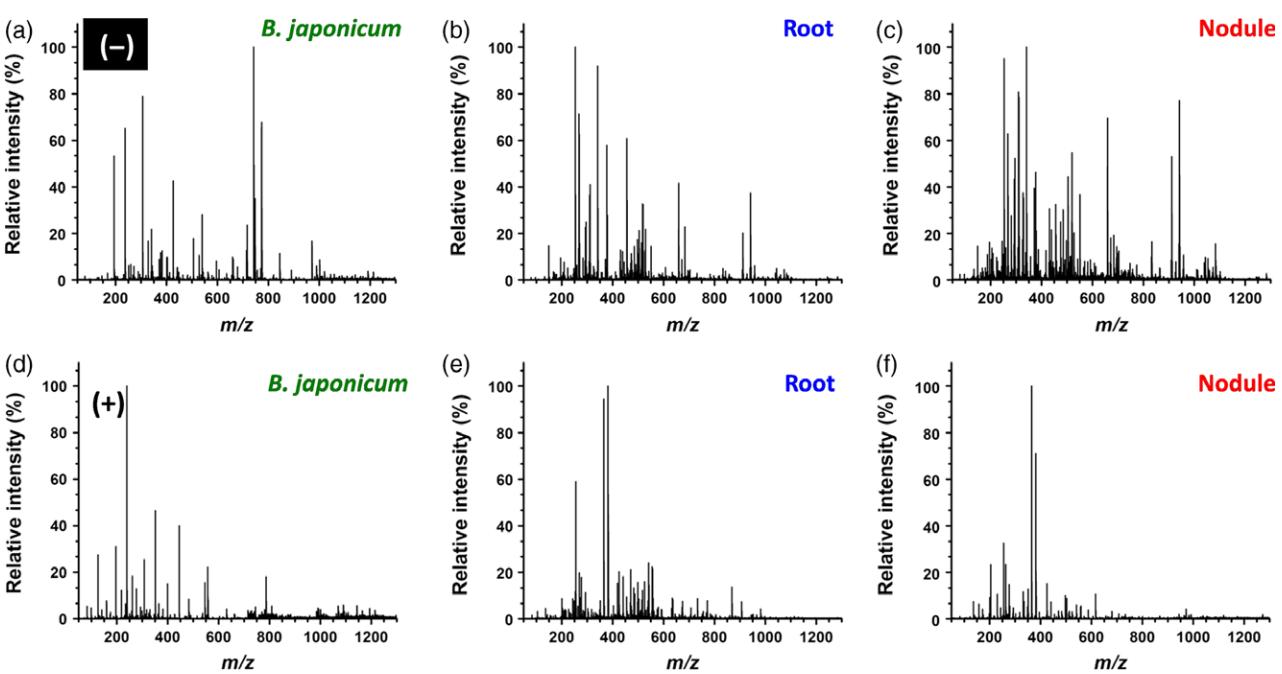

Figure 2. Metabolic profiling and comparison of root nodule components and using LAESI-MS.
Representative LAESI mass spectra of (a, d) free-living *B. japonicum* cell pellets, homogenized (b, e) uninfected soybean roots, and homogenized (c, f) soybean root nodules in (a–c) negative and (d–f) positive ion mode. [Colour figure can be viewed at wileyonlinelibrary.com].

other direct laser-ablation-based analytical methods utilized in plant biology (i.e., laser-ablation inductively coupled plasma MS). It has been demonstrated that the internal energy induced by the mid-IR laser-ablation process does not significantly alter molecular survival yields (i.e., producing minimal molecular fragmentation), and that ions produced by LAESI are essentially indistinguishable from that of stand-alone ESI (Nemes *et al.*, 2012). However, the in-source fragmentation that does occur during the LAESI process is primarily due to electrospray ionization. Xu *et al.* recently demonstrated the extent of in-source fragmentation of ESI on yeast metabolites, illustrating that metabolite misinterpretation is possible using any ESI based analysis (e.g., LC-MS or DESI). We analyzed standards of metabolites detected in our soybean samples with ESI and LAESI-MS to determine the level of in-source fragmentation of these specific molecules (Figure S1). Here, we found that the laser-ablation process caused additional fragmentation of only a few species compared with ESI alone.

Statistical data analysis reveals unique metabolites

In order to identify unique molecular ions and determine their significance within each sample group, we employed a statistical analysis approach. Hierarchical clustering, in the graphical representation of a heat map, provided visualization of the mass spectral features, as displayed in the rows, and differences among the free-living rhizobia, root nodules, and uninfected root samples, as depicted in the columns. (Figures 3a and S2a show positive and negative ion mode results, respectively.) The column and row dendrograms revealed that the root nodule and uninfected root shared a secondary node, indicating closer spectral similarity compared to free-living rhizobia.

Visual comparison of a representative mass spectrum (Figure 2) of each sample group can be used to establish discriminating spectral features. However, to determine the spectral features that maximized the covariance between sample types, we employed PLS-DA, which provided group-specific metabolites based on a larger sampling population (Figures 3b and S2b, positive and negative ion mode results, respectively). Both scores plots showed significant covariance based on mass spectral differences, which revealed a large degree of separation in the three sample groups. In positive ion mode, the most significant separation, component 1 (*x*-axis of Figure 3b), captured 48% of the covariance, which presented variables that discriminated between the plant-based samples and the free-living rhizobia. On the other hand, component 2 (*y*-axis of Figure 3b) captured 19% of the covariance and illustrated the molecules that differentiated the infected and uninfected plant tissue. From the loading plots, we constructed box-and-whisker graphs to determine the unique molecular makeup of each sample type (Figure 3c). For example, [PE (16:0/18:1)-H]$^-$ at *m/z* 716.516 showed the highest abundance in the free-living rhizobia, whereas [adenine+H]$^+$ at *m/z* 136.062 was mainly detected in the root nodule. Several ions were present in all three groups, but were more abundant in one group compared to the others. For example, [disaccharide+Na]$^+$ at *m/z* 365.106 was present in the root nodule and the uninfected root, but was more abundant in the latter. Molecules potentially related to BNF would be expected to be enriched in the root nodules relative to, for example, the free-living rhizobia. Here, we found [heme *B*]$^+$ at *m/z* 616.179 was detected in higher abundance within the root nodule samples than in the free-living rhizobia, and it was not detected in the uninfected root. This likely reflects the very high abundance of leghemoglobin in the nodule.

Enhanced molecular coverage by IMS

The integration of IMS into the experimental workflow provided an additional separation dimension, which allowed for the detection of isobaric compounds and the ability to elucidate the CCS values based on DT of each molecular ion. Furthermore, the combination of CCS values with the accurate mass and tandem MS measurements provided increased molecular coverage of detected ions and a greater confidence in their identification. This enhancement was illustrated in the volcano plots (Figure 4) comparing the ions detected in the root nodule and uninfected root samples. Without this separation step, 603 spectral features were detected in the plant tissue samples (Figure 4a), of which 257 were significantly more abundant in the uninfected root tissue (i.e., arbitrary cut-off value was 1 and -1 in the $\log_2$ scale corresponding to >2 and <0.5-fold change and significance *P*-values <0.05), and 108 were significantly more abundant in the root nodules. By incorporating IMS with the MS (Figure 4b), the total number of spectral features increased by nearly double to 1000. Moreover, 255 features were significantly more abundant in the uninfected root tissue than in the root nodule, and 263 features were vice versa. Overall, the addition of IMS resulted in a gain of 153 differentially abundant spectral features. Investigation into these spectral features revealed several promising BNF candidates that were significantly more abundant in the root nodule (Figure 4c), including [glutamate-H]$^-$ at *m/z* 146.049 and [acetyl glutamic acid-H]$^-$ at *m/z* 188.058 (with fold changes of 3.9 and 9.9, respectively). Metabolites that were significantly more intense in the uninfected root samples included [dihydroxyflavanone-H]$^-$ at *m/z* 253.052 with a fold changes of -5.8.

The ability to detect isobaric ions was illustrated by examining the nominal mass at *m/z* 203.055 $\pm$ 0.005, which prior to IMS analysis was not considered significantly different in intensities in either the root nodule or in the uninfected root (Figure S3a). The addition of the IMS step revealed two peaks were present, one peak with *m/z*

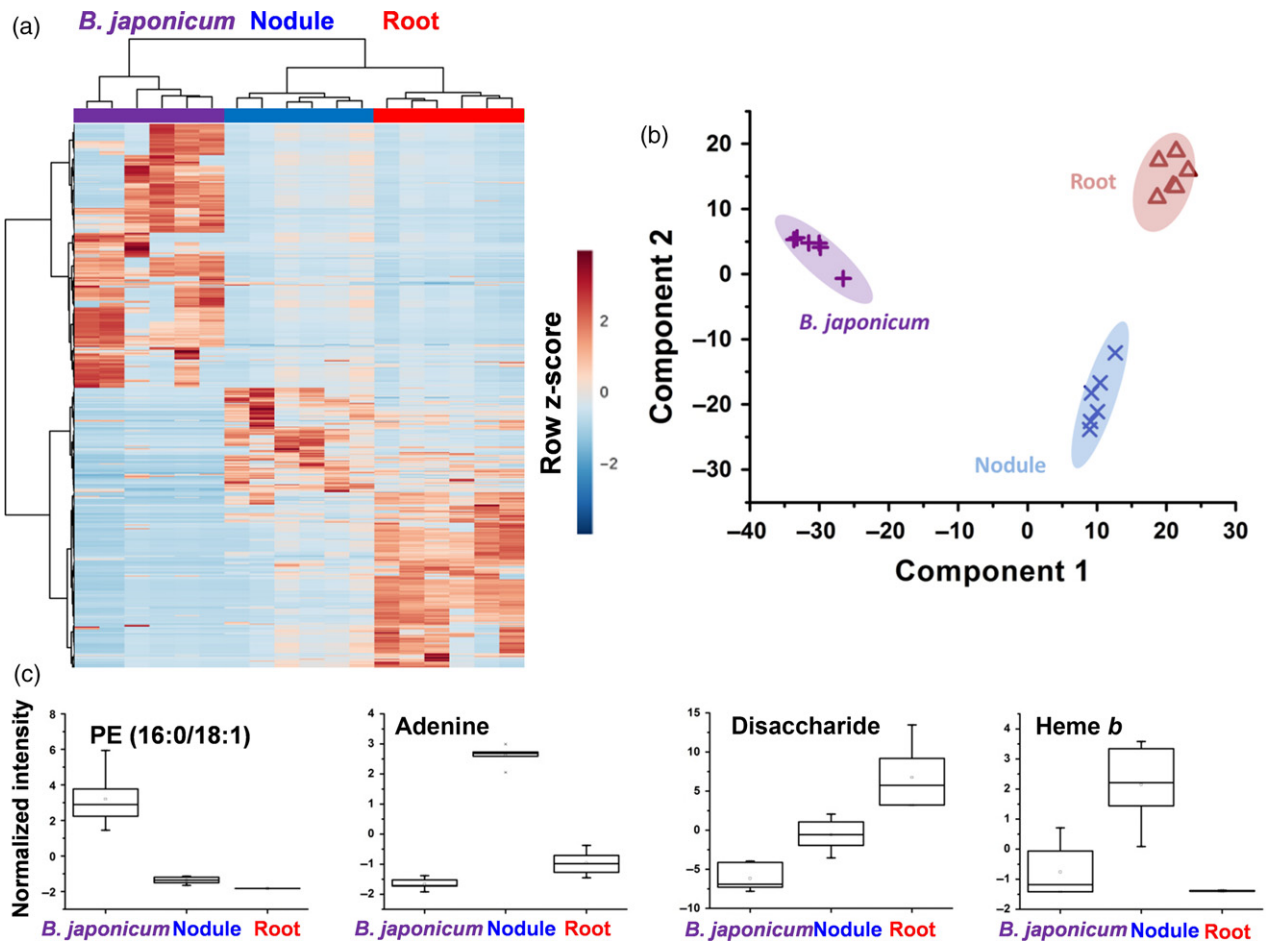

Figure 3. Measuring spectral variance within sample replicates and between sample groups.
(a) Heat map illustrating the major spectral difference based on normalized positive ion spectra, where each column is a spectrum and each row is an *m/z*. The color for the samples of the heat map represents the relative abundance of metabolites: red is greater relative abundance and blue is lower relative abundance.
(b) Scores plot from PLS-DA of the spectra, which were used to assist in identifying minor species that are significant in each system with a 95% confidence. The corresponding loadings plots from PLS-DA of the spectra were used to identify peaks of interest.
(c) Relative abundances of four significant species as identified from the loadings plots.

203.053 and another at *m/z* 203.057, with CCS values of 143 and 139 Å^2, respectively (Figure S3b,c). An in-house CCS metabolite constructed library consisting of 407 unique small molecules (Mass Spectrometry Metabolite Library of Standards, IROA Technologies, Bolton, MA, USA) was used to match potential compounds. The identification was based on accurate mass, CCS value, and tandem MS by LAESI–IMS–MS using the same instrumental conditions for both the standards and the biological tissues. Comparison of these two isobaric ions with our in-house library suggested that the identifications were theophylline and a monosaccharide with CCS percent error rates of 2.1 and 0.7%, respectively. Further, we found theophylline was significantly more abundant in the root nodules, whereas the monosaccharide showed greater abundance in the uninfected root samples. Overall, IMS increased the molecular coverage for the detection of biomolecules found in the nodule and root groups.

To visualize the large datasets produced by IMS–MS, we constructed DT versus *m/z* plots (Figure 5). These 3D plots showed an ion's measured *m/z*, color intensity proportional to relative abundance, as well as its DT values, which were measured on the order of msec illustrating the high-throughput analysis. The separation of molecules in IMS is based on an ion's physical size and shape, which affects the time it takes to pass through the drift cell. As expected, in the lower *m/z* regions we observed shorter DT (e.g. [cyclohexylammonium+H]$^+$ at *m/z* 100.114, DT of 1.39 msec and [choline+H]$^+$ at *m/z* 104.110, DT of 1.36 msec). Conversely, larger *m/z* compounds had longer DT (e.g., [heme *B*]$^+$ at *m/z* 616.179, DT of 5.43 msec and [soyasaponin αg+H]$^+$ at *m/z* 1085.546, DT of 11.88 msec). These DT values can be converted to the more universally accepted CCS values, which could be used to classify groups of molecules (see Figure 4e) by plotting the individual compound CCS values with their measured *m/z* values.

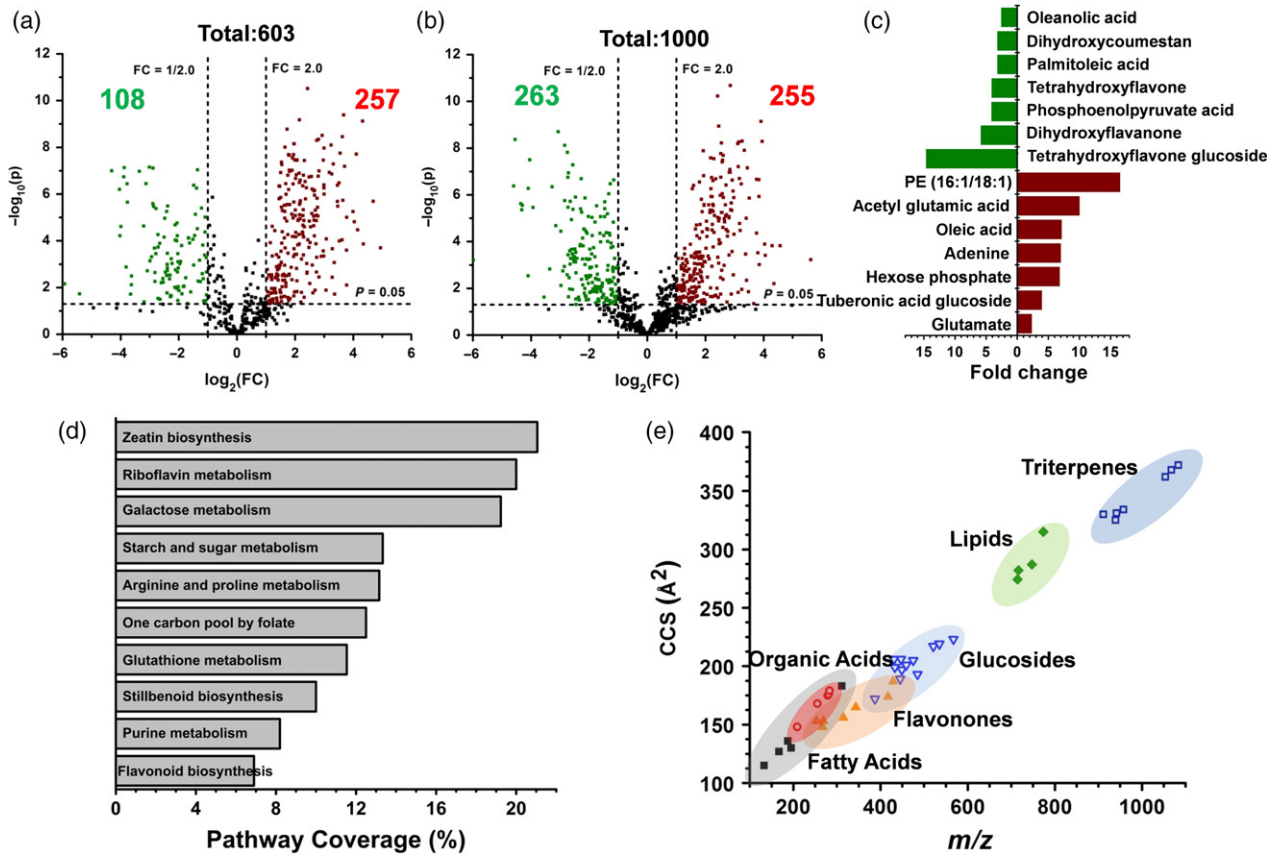

Figure 4. Exploring the benefits of IMS pre-mass analysis, where it increased detected metabolite coverage, provided higher confidence in molecular identification of value for exploring active metabolic pathways, and offered insights into the classes of detected unknown molecules.
(a, b) Volcano plots comparing major differences between negative ion mode species detected in the (green) uninfected soybean roots and (red) root nodules (a) without IMS and (b) with IMS. The addition of IMS increased the number of significant spectral features from 365 to 518.
(c) Highlight of significant molecules from root nodule and uninfected root that have a significance of a least a fold change of two and *P*-value < 0.05, where down-regulated in the root nodule is in green and up-regulated is in red. Refer to Table S1 for identification.
(d) To ascertain active metabolic pathways detected within the intact nodule by LAESI–IMS–MS, a network approach was employed. Using the PathwayViewer installment within the SoyKB web resource, a total of 112 tentatively identified metabolites that exhibited a *P*-value < 0.05 and a fold change >2 were considered for analysis. The top 10 impacted pathways revealed significant involvement, several of which could be directly correlated with BNF.
(e) Separation and classification of detected molecules by IMS by comparing CCS and *m/z* values for the different classes of compounds.

For example, in negative ion mode, the fatty acid CCS values exhibited a range of 148–179 Å^2; flavonones ranged from 148 to 187 Å^2; and larger molecules such as triterpenes covered a range of 330–372 Å^2. The CCS values for glucosides ranged between 172 and 223 Å^2. They showed some overlap into the flavonone region, but because of their unique linear trends both groups were resolvable from one another.

Within these DT versus *m/z* plots, we found that a typical root nodule plot contained approximately 667 peaks and that the uninfected root showed approximately 462 peaks in positive ion mode (Figure 5a,b). For spectral comparison of two DT versus *m/z* plots, we constructed a fusion map between the root nodule (red) and uninfected root (green) samples (Figure 5c). A total of approximately 226 differentially abundant peaks was detected, including [heme *B*]$^+$ and [adenine+H]$^+$ that had previously been identified as nodule-linked compounds based by our statistical analysis (noted earlier). An illustrated advantage of this fusion plot is the ability to elucidate near isobaric ions that would have otherwise spectrally overlapped. Investigation within the DT of 5.03 msec from the fusion map revealed [dehydrosoyasaponin+Na]$^+$ at *m/z* 963.495 and [triterpene glycoside+Na]$^+$ at *m/z* 971.512 localized to the nodule (Figure 5d). By comparison, within the DT of 9.78 msec, we observed the triterpene [soyasaponin I+H]$^+$ at *m/z* 943.527 and [soyasaponin I+Na]$^+$ at *m/z* 965.520 in the uninfected root (Figure 5e). The highlighted zoom-in region within the fusion map showed these two different DT ranges and the corresponding *m/z* range. There were overlapping spectral features (Figure 5f), but were resolvable with IMS.

Lastly, the use of IMS provides an orthogonal analysis method valuable to the four-level classification system for metabolite identification developed by the Metabolomics Standard Initiative (Sumner *et al.*, 2007). This classification

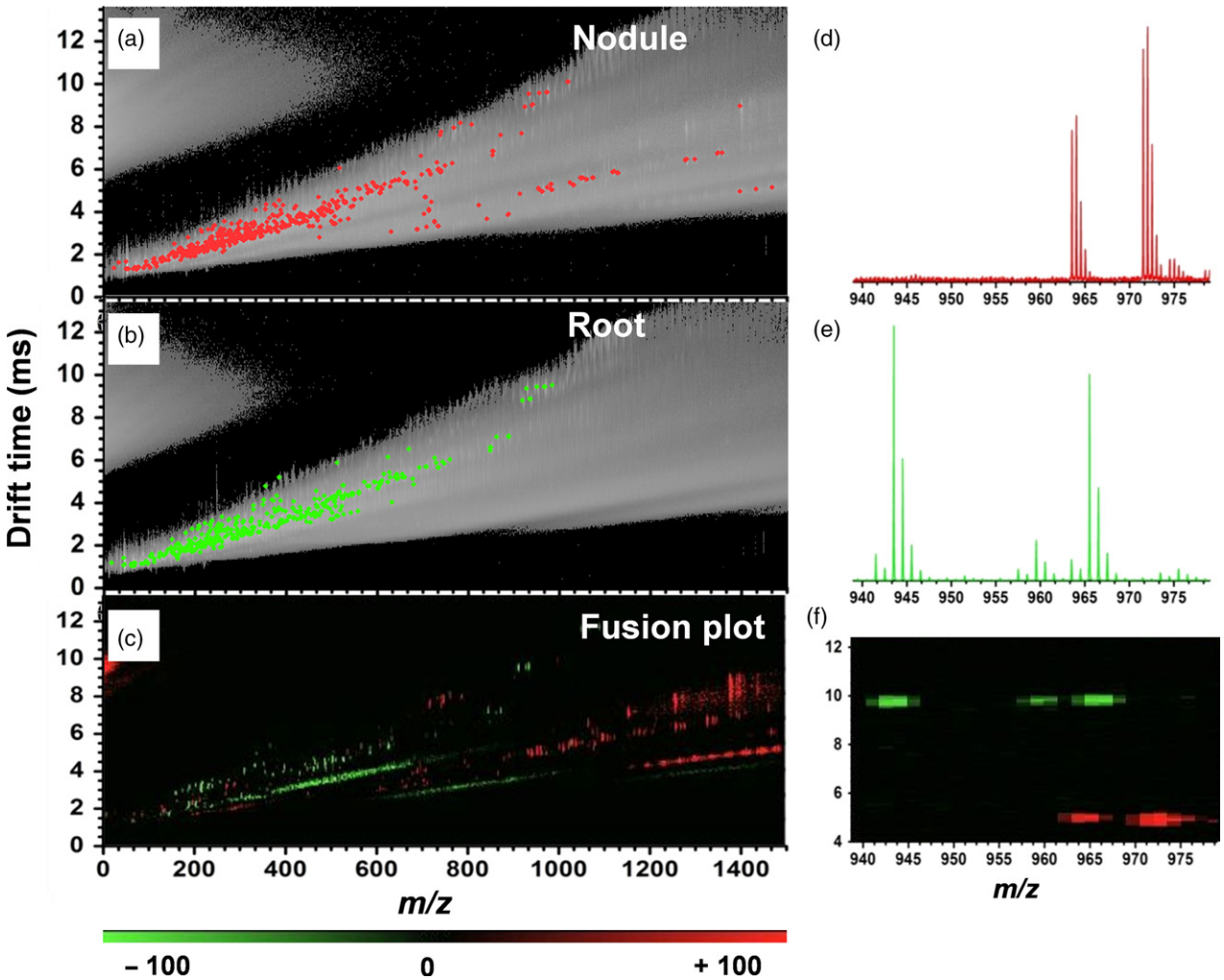

Figure 5. Visualizing IMS-MS data generated from infected and uninfected root samples.
(a–c) A representative LAESI–IMS–MS drift time (DT) versus *m/z* plot of (a) root nodule and (b) uninfected root sample in positive ion mode. The two former DT versus *m/z* plot where combined into a (c) fusion plot highlighting IMS spectral differences between the (red) root nodule and (green) uninfected root.
(d–f) A highlighted mass spectral view of (d) root nodule (DT = 5.03 msec) and (e) uninfected root (DT = 9.78 msec) of the selected (f) fusion plot covering the mass region between 935 and 980 *m/z*, and spanning a DT range of 4–12 msec revealed separation of sample-dependent ions.

system was designed to standardize the reporting of metadata in order to provide empirical and biological context to data, and to facilitate ease in comparing data. We employed this metabolomics community-adopted approach, and found that of the 107 tentatively assigned compounds in this study, 21 were identified as level 1, 32 were putatively annotated as level 2, and 54 were putatively characterized as level 3 (Table S1). The criteria for a level 1 compound classification includes two independent and orthogonal data streams in the form of accurate mass and both the measured tandem MS spectra and CCS values. We compared these data streams with reference standards analyzed under identical conditions. Compounds that were putatively assigned as level 2 were based on accurate mass and tandem MS spectra as compared to external reference standard databases. Lastly, level 3 characterization was determined only by matching accurate mass data with reference masses.

Intact soybean nodule depth profiling

We performed depth profiling of intact soybean nodules by setting the laser to low repetition rates and matching the laser pulses to the scan rate of the mass spectrometer. Here, we collected a single mass spectrum at each laser shot by setting the laser pulsing and MS scanning to 1 Hz. This procedure provided spatial information about the molecular composition of the anatomical layers of the soybean root nodules (Figure 6). An average ablation crater of approximately 150 μm in diameter (Figure 6a) was created by focusing the laser into the meristem side of the root nodules. Inspection and construction of a *z*-stack using an optical microscope revealed that the first 20 shots removed

approximately 90 μm and of 40 shots removed approximately 163 μm, suggesting that each shot removed approximately 4 μm of the dry epidermal layer of the root nodule. To penetrate the epidermal layer required approximately 45 individual laser shots, resulting in the removal of approximately 183 μm of material. Continued ablation past the epidermal layer resulted in sampling the inner infected zone of the nodule, which contained the bacteroid cells and is the primary location of BNF.

We localized specific ions to the different layers and tracked them by observing the ion intensity over the number of laser shots (Figure 6b). For example, monitoring [soyasaponin βg+H]$^+$ at *m/z* 1069.551 revealed high abundance in the first 45 laser shots after the laser was pulsed, followed by diminished signal that indicated its presence only in the outer layer of the nodule. Within the same experimental run, ions localized to the infection zone (e.g., [heme *B*]$^+$ at *m/z* 616.179) increased in ion intensity after the epidermal layer was ablated away. Overall, approximately 180 spectral features were present in the outer layer and approximately 112 features to the infection zone (Figure 6c,d, respectively). Molecular species tracked to the outer layer included [soyasaponin βg+H]$^+$ at *m/z* 1069.551, [dihydroxy methoxyflavone+H]$^+$ at *m/z* 285.071, and [trihydroxyflavone+H]$^+$ at *m/z* 271.063. Within the infection zone several ions were localized, which included [heme *B*]$^+$ at *m/z* 616.179, [adenosine+H]$^+$ at *m/z* 268.104, and [riboflavin+H]$^+$ at *m/z* 377.153. There was an overlap of approximately 76 ions present in both the outer and inner layers. For example, [adenine+H]$^+$ at *m/z* 136.062, [choline+H]$^+$ at *m/z* 104.110, [cyclohexylammonium+H]$^+$ at *m/z* 100.114, [hydroxy methoxyisoflavone+Na]$^+$ at *m/z* 309.039, and [tetrahydroxyflavone glucoside+Na]$^+$ at *m/z* 471.093 were some of the several ions detected throughout the entire nodule anatomy.

Lateral profiles of sectioned root nodules

In order to confirm the localization of molecules to the different anatomical layers of the intact root nodules, we used LAESI–MS to laterally profile 60 μm thick nodule sections. Here, we sampled two regions, the epidermal layer and the center of the infection-zone of the nodule

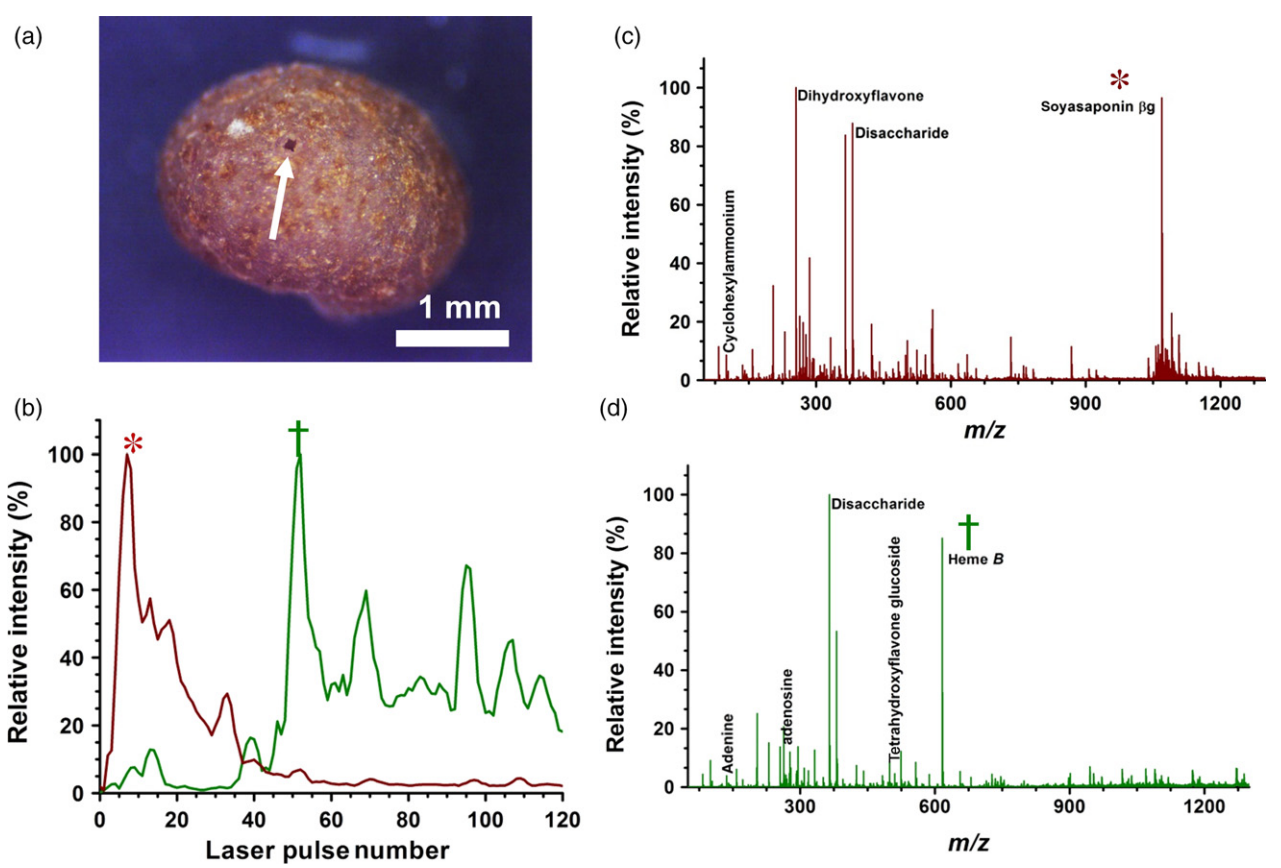

Figure 6. Example of a LAESI-MS depth-profiling analysis of a soybean root nodule in positive ion mode.
(a) Optical image of the soybean nodule after depth profiling. Here, a small ablation crater with a diameter of 150 μm can be seen (arrow acts as guide), where the meristem side of the nodule was depth profiled.
(b) The intensities of *m/z* = 1069.56 (red) and 616.178 (green) over number of laser pulses. The number of laser pulses was indicative of the nodule layer sampled.
(c, d) (c) Average mass spectrum from the outer layer for 1–45 laser pulses and (d) average mass spectrum from 50 to 90 laser pulses.

(Figure 7). We targeted three laser shots at a single sampling area to ensure that all material was removed. This resulted in ablation spots approximately 300 μm in diameter. When the outer region was sampled, we confirmed the presence of several epidermal-related ions, including [soyasaponin βg+H]$^+$ at *m/z* 1069.551 and [trihydroxyflavone+H]$^+$ at *m/z* 271.063, as shown in the intact depth nodule experiments. As for the infection zone, [heme *B*]$^+$ at *m/z* 616.179, [adenosine+H]$^+$ at *m/z* 268.104, and [jasmonoyl aminocyclopropane carboxylate+K]$^+$ at *m/z* 332.121 was confirmed to be localized to the inner anatomy of the nodules. Several monosaccharides (e.g. [monosaccharide+Na]$^+$ at *m/z* 203.051) and flavonones (e.g. [dihydroxyflavone+H$^+$] at *m/z* 255.063) were detected in both the outer and inner region.

DISCUSSION

In this contribution, we demonstrated the utility of using the ambient ionization ability of LAESI coupled with IMS–MS to explore the symbiotic relationship between free-living rhizobia and soybean plants and we overcame the significant restriction of limited spectral separation in LAESI–MS. This high-throughput technology provided an *in situ* analysis method capable of revealing differentially regulated metabolites linked to each component of the symbiosis. We were able to detect over 700 species per sample group and we identified 107 metabolites based on their measured *m/z*, tandem MS, and calculated CCS values (Table S1). These identified molecules included fatty acids, organic acids, flavonones, glucosides, lipids, sugars, growth factors, and triterpenes. Furthermore, we detected well-known metabolites linked to the BNF process within the soybean nodules (Schubert, 1986). Using statistical data analysis methods, we determined which of these compounds were unique to free-living rhizobia, uninfected roots segments, and the root nodules (i.e., a physiological transformation based on the combination of the former two components), all without the need for extensive sample preparation. Lastly, we were able to spatially locate analytes within whole-root nodules by depth profiling these samples.

By including IMS into our analysis workflow, we were able to distinguish isomers and molecules with very similar *m/z* values – ions typically only distinguishable by high mass resolving power Fourier transform-based MS (Shaw *et al.*, 2016). Moreover, the statistical significance of these isobaric ions was revealed between samples, as was noted in the case of detection a monosaccharide and theophylline, which exhibited higher abundances in the uninfected root and root nodule, respectively. Another advantage of IMS is that it allowed for tentative identification of what class an unknown compound belonged to, as indicated by the CCS range it fell within. These separations were on the order of msec, overcoming the limitation of fluid chromatography techniques prior to ionization (e.g., GC and LC), which are common bottlenecks of MS-based methods.

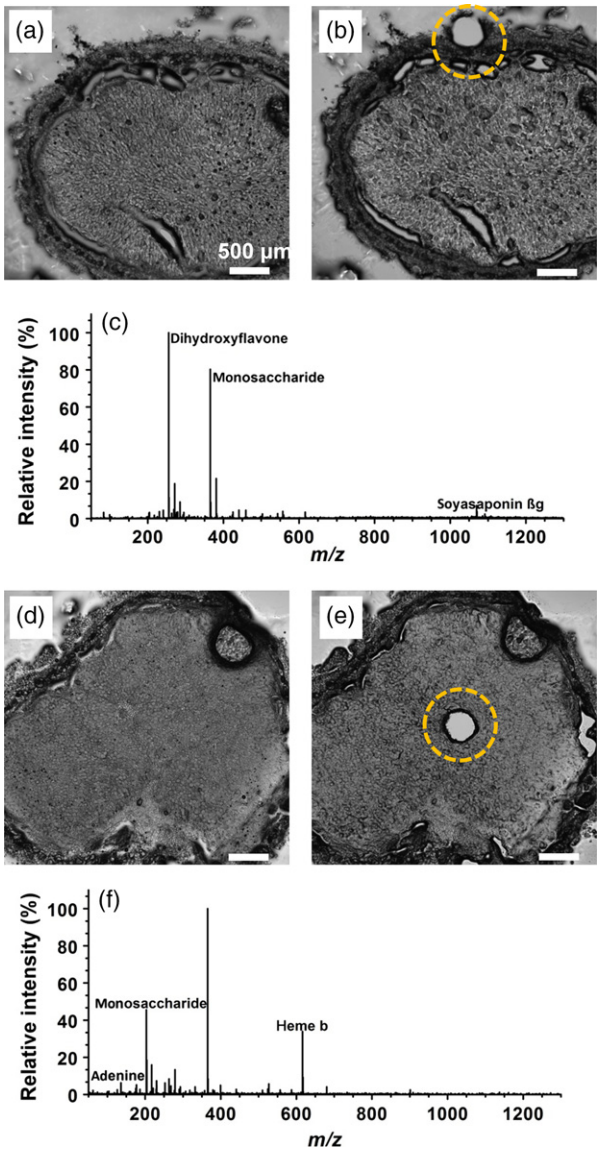

Figure 7. Lateral profiling of 60 μm thick soybean root nodule sections by LAESI–MS, which were performed in an effort to validate location of specific analytes.
(a, d) Bright-field images of the nodule section before LAESI–MS analyzes.
(b, f) Corresponding bright-field images after LAESI–MS analysis, respectively.
(c, f) are the corresponding mass spectra from the areas analyzed in (a) and (e), respectively. Here, MS was performed in positive ion mode for direct comparison with the data seen in Figure 6. [Colour figure can be viewed at wileyonlinelibrary.com].

By using LAESI–IMS–MS, we detected a wide range of compounds with varied polarities and concentrations within a single experiment. As such, we were able to detect an array of molecules, in a label-free fashion, needed to maintain efficient symbiosis. Many of these

molecules could be associated with important biochemical processes and their related transformations taking place within the complex regulatory networks of the uninfected roots and root nodules. For instance, the large class of carbohydrates accounts for numerous roles within plants. In particular, sugars and polysaccharides have an essential role in plant metabolism, development, physiology, and storage. Our analysis revealed a high presence of monosaccharides, disaccharides, and trisaccharides within the plant systems (e.g., the uninfected roots and root nodules), as well as in low abundance in the free-living rhizobia. This correlated well with known literature that showed similar metabolites within plant roots and nodules (Gibson, 2000; Lardi *et al.*, 2016). We also detected the 5-carbon monosaccharide ribose in the plant systems, and we detected its products in the form of energy metabolic coenzymes in the free-living rhizobia. The health of a cell can be expressed based on the energy stored within an adenylated system by recording the levels of AMP, ADP, and ATP. The adenylated energy charge expressed as AEC = (ATP + 1/2 ADP)/(AMP + ADP + ATP reveals the health of a cell using a range from 0 to 1 (from less to more healthy, respectively) (Bomsel and Pradet, 1968). Within the free-living *B. japonicum*, we determined the AEC to be 0.67 ± 0.06 (accounting for in-source fragmentation of ATP). That is in agreement with previous studies that found similar AEC values for healthy nitrogen-fixing bacteria (Upchurch and Mortenson, 1980). Previous NMR efforts were unable to detect these molecules in the free-living forms (Vauclare *et al.*, 2013).

Flavonoids play an important role in symbiotic plant–rhizobia processes. A signaling cascade starts with the secretion of these compounds from the plant roots recognized by the rhizobia, leading to the nodule formation (Rolfe, 1988; Subramanian *et al.*, 2007). In our analysis, we were able to detect these important bioactive molecules in both the uninfected roots and root nodules. However, taking into account biological and statistical significance (fold change >2 and *P*-value < 0.05, respectively), we observed that the flavonoids were present at higher abundance in the uninfected root compared to the root nodule samples. This was as expected since these molecules act as chemical-attractant signals, drawing rhizobia to their host roots.

Legumes that undergo BNF synthesize symbiotic leghemoglobin proteins, which are essential for nodule development and growth. In particular, these nitrogen and oxygen carrier hemoproteins provide the bacteroid cells with an adequate supply of oxygen for respiration. In our statistical analysis of homogenized uninfected root, root nodules, and free-living rhizobia cell pellets, we detected heme *B* in the root nodule samples and the free-living rhizobia. Previously, it was suggested that free-living rhizobia produce small amounts of heme (Nadler and Avissar, 1977). This correlated well with our findings of heme *B*, which the root nodule expressed the largest abundance, followed by the free-living rhizobia. We did not detect heme *B* in the uninfected root samples.

Alternative biomolecules important in BNF play secondary roles, such as being defensive mechanisms against pathogenic microbes and herbivores (e.g., triterpenoid saponins) (Bais *et al.*, 2006; Zhuang *et al.*, 2013). This diverse group of natural products is widely abundant in plants (Achnine *et al.*, 2005; Vincken *et al.*, 2007), and is involved with a wide range of bioactivities, including acting as agronomic and ecological plant defense mechanisms (Sparg *et al.*, 2004; Field and Osbourn, 2008). They are also involved in commercial applications such as cosmetics, pharmaceuticals, and industrial biotechnology areas (Thimmappa *et al.*, 2014). Furthermore, the role of triterpenoid saponins within the symbiotic interactions of legumes and rhizobia is largely unknown. The main triterpenoid saponins detected in soybean plants are a β-amyrin-derived oleanane-type known as soyasaponins, which are divided into two classes, soyaspogenol A and soyasapogenol B (Kitagawa *et al.*, 1988). We were able to detect seven different soyasaponins in both the uninfected root and root nodules, as well as the abundant soyasaponin Aa and soyasaponin βg in both positive and negative ion modes.

We also demonstrated that LAESI could be used to spatially elucidate the metabolite composition of different anatomical regions of the intact root nodules with minimal sample preparation by depth profiling intact nodules. Our demonstration did not involve an exhaustive spatial analysis of nodules, but rather a 'proof of concept' by lateral profiling of root nodules sections to confirm the results of our depth-profiling experiments. This allowed us to establish that depth profiling of whole-root nodules would provide location-specific metabolic information without the need for any sample preparation. From these results, the role of metabolites could be revealed based on their location within the nodule. Specifically, in the epidermal layer of the root nodule, we detected many molecules that had a defensive role in the plant physiology (e.g., triterpenoid saponins). This matched with a previous report that utilized a β-glucuronidase assay of saponin-deficient 1 (*Sad1*) promoter that revealed the localization of saponins to the meristematic and outer regions of indeterminate nodules in *Medicago truncatula* (Kemen *et al.*, 2014). In the inner infection zone, we detected molecules involved in BNF (e.g., heme *B*), where leghemoglobin has been associated with the reddish color of the central infected zone of the nodules (Brewin, 1991).

Pathway analysis of high-abundant metabolites detected from the root nodules revealed several important networks associated with BNF (Figure 4d). Here, we took statistically significant metabolites detected from the homogenized nodules and correlated them to their corresponding

compound name based on KEGG identification numbers to input within the pathway Viewer analysis tool (SoyKB) based on KEGG pathways. In total, 112 metabolites met these parameters and were used for the analysis. However, we did not include a significant fraction of these metabolites (out of the 112) for analysis as they had no representative KEGG database ID. Thus, our coverage only included a small representation. Nevertheless, we still obtained meaningful information with the top-10 pathways containing approximately 7–21% coverage, with some of these pathways related to BNF. For instance, the highest percentage coverage was the zeatin biosynthesis four of 19 metabolites measured), which includes the cytokinin family as a class of phytohormones. These molecules play a significant role in plant growth and development, as well as in nodule organogenesis in the root cortex (Murray *et al.*, 2007; Oldroyd and Downie, 2008). The second highest pathway coverage was the riboflavin metabolism (two of 10 molecules detected), which is biosynthesized in plants and bacteria (Bacher *et al.*, 2000) as a direct precursor of the flavin cofactors (McCormick, 1989). Root-colonizing bacteria secrete riboflavin as a significant ecological factor in host-plant root colonization and communication by rhizobia, root respiration and nodulation, and in host-plant shoot growth (Schwinghamer, 1970; Yang *et al.*, 2002; Yurgel *et al.*, 2014). Interestingly, we obtained a pathway coverage of 8% purine metabolism (five of 61 species observed), which is involved in BNF. Purine *de novo* biosynthesis consists of amino acids and nucleotides, like the molecules we detected (glutamine, adenine, and guanine). These were then converted to monophosphates, followed by oxidation to xanthine, and lastly to allantoin, a ureide (Zrenner *et al.*, 2006). The production of ureides in soybean from this purine metabolism plays a huge role in BNF, since ureides provide a nitrogen source that can be transported from the nodule and consumed in other parts of the plant (Smith and Atkins, 2002; Baral *et al.*, 2016). This untargeted approach of metabolite profiling performed by LAESI–IMS–MS demonstrated the ability to detect these amino acids, nucleotides, and fixed nitrogen sources from purine metabolism in the nodules in a high-throughput fashion. Overall, we were able to detect multiple pathways associated with the BNF process within soybean nodules. This ambient ionization method can be translated to other biological model systems for rapid analysis of metabolites and affected biochemical networks.

In conclusion, our results illustrate the feasibility of LAESI–IMS–MS as a high-throughput untargeted technique for the detection of metabolites, lipids, and other small molecules from intact root soybean nodules. We elucidated the origin of the detected biomolecules from analyzing uninfected root segments and free-living rhizobia. Further analysis, incorporating internal standards into our LAESI–IMS–MS workflow, can provide quantitative information about metabolite concentrations between the different compartments and biological components of the root nodules. This is done by compensating for known ion suppression and ionization efficiency issues in MS analysis (Annesley, 2003; Bilkey *et al.*, 2016). With the incorporation of IMS, we expanded the coverage of the differentially abundant metabolites, and ion mobility separation also assisted in the detection of isomers. Depth profiling of intact root nodules revealed the location of metabolites in specific regions of the sample and provided context to their biological significance. Furthermore, we gained this spatial information without the need for extensive sample preparation, which typically requires expensive equipment (e.g., microtome), multiple time-consuming steps (e.g., preservation and embedding), and skilled technicians. The separation timescale of IMS, in conjunction with the *in situ* sampling ability of LAESI, offers a high-throughput screening method for analyzing native samples. Finally, the potential applications of this work could lead to rapid phenotyping of plant tissues, a topic of considerable recent interest.

EXPERIMENTAL PROCEDURES

LAESI–IMS–MS instrumentation

A quadrupole time-of-flight mass spectrometer with a traveling wave IMS system (Synapt G2S; Waters, Milford, MA, USA) was retrofitted with a homebuilt LAESI source (Shrestha and Vertes, 2014). A mid-IR laser source (IR Opolette HE 2731; Opotek, Carlsbad, CA, USA), tuned to a wavelength of 2.94 μm, delivered 7 nsec laser pulses with repetition rates ranging between 1 and 20 Hz. Using a plano-convex ZnSe lens (Infrared Optical Products; Farmingdale, NY, USA) with a 75 mm focal length, the laser beam was focused onto the sample. A Peltier stage was used to maintain the sample temperature at approximately 0°C to reduce sample degradation in the homogenized plant tissue and cell pellet experiments. Following each laser pulse, an ablation plume was formed that was intercepted by an electrospray aligned on-axis with the MS orifice. The spray solution was supplied through a stainless steel emitter (MT320-50-5-5; New Objective, Woburn, MA, USA) at a flow rate of 500 nL/min using a syringe pump. For positive ion mode, the electrospray solution composition was 1:1 (v/v) MeOH:water with 0.1% acetic acid and the voltage on the emitter was kept at +3300 V. In negative ion mode, the spray solution was a 2:1 (v/v) mixture of MeOH:$CHCl_3$ and −2700 V was applied to the emitter. For all experiments, IMS was performed with nitrogen drift gas, supplied at 90 mL/min and 3.35 bar, and the delay coefficient was set to 1.41 V. The height and velocity of the traveling wave were set to 40 V and 650 m/sec, respectively.

LAESI–IMS–MS data acquisition

Bradyrhizobium japonicum cell pellets and homogenized plant tissue. Cell culturing of *B. japonicum* and growth of soybean plants (*Glycine max* Williams 82) are described in more detail within Experiment Procedures S1. For bulk rhizobia analysis, post centrifugation and washing, the cell pellets were resuspended in 20 μL of deionized (DI) water and 10 μL of the suspension was pipetted onto a microscope glass slide and analyzed directly. For the homogenized plant tissue analysis,

approximately 10 mg of the uninfected soybean roots or soybean root nodules were placed into 2 mL vials that contained 40 μL of DI water. The vials were placed on ice and the contents were probe sonicated (QSonica Q125, Newton, CT, USA) for 30 sec with 1 sec pulse durations, at an amplitude of 30%, followed by 2 sec idle time. For LAESI–IMS–MS analysis, 10 μL aliquots of the sonicated material were placed on a glass microscope slide.

Intact and sectioned soybean root nodules. Frozen intact nodules were first placed into sterile DI water for approximately 2 sec and blotted dry with a lint-free tissue. Root nodules were then immobilized onto a standard microscope slide using double-sided tape. The laser and mass spectrometer were both scanned at a repetition rate of 1 Hz, providing mass spectra from single laser pulses as they ablated through the different layers of the nodules. Sampling was complete when analytes were no longer detected. Cryosectioning was performed using a cryostat microtome (CM1800; Lecia Microsystems Inc., Nussloch, Germany) set to −10°C. Whole nodules were immersed in 2.5% carboxymethyl cellulose (CMC) embedding medium in a mounting tray, and placed inside the cryostat for 30 min. Once frozen, the excess CMC around the sample was removed with a scalpel. The sample block was then affixed on a specimen mount with a few drops of CMC. Root nodule sections of 60 μm thickness were thaw-mounted onto a microscope slide. Freshly sectioned root nodule samples were imaged immediately in a microscope (IX71; Olympus, Tokyo, Japan), analyzed by LAESI–IMS–MS, and then reimaged in a microscope to confirm the locations of the ablation craters. Detailed information regarding data and statistical analysis can be found in the supporting Experiment Procedures.

ACKNOWLEDGEMENTS

This material is based work supported by the U.S. Department of Energy, Office of Biological and Environmental Research under award number DOE-FOA-0001192. S.A.S would also like to acknowledge the Achievement Rewards for College Scientists Foundation, Inc. for a scholarship award. Additional support was provided by University of Missouri's Gus T. Ridgel Fellowship and George Washington Carver Fellowship (B.J.A). We would like to thank Yaya Cui for his help with growing and inoculating numerous soybean plants.

CONFLICT OF INTEREST

The authors declare no conflict of interest.

SUPPORTING INFORMATION

Additional Supporting Information may be found in the online version of this article.

Figure S1. Extent and annotation of in-source fragmentation of standards by LAESI-MS of metabolites detected in soybean nodules.

Figure S2. Multivariate statistical analysis of negative ion mode spectra for nodules, uninfected root segments, and free-living rhizobia.

Figure S3. Separation of isobaric ions by IMS, which revealed statistically significant differences between nodules and uninfected roots.

Table S1. Putative annotation of compounds detected from root nodules, uninfected root segments, and free-living rhizobia.

Experimental Procedures S1. Cell culture and plant growth, and LAESI–IMS–MS data analysis.

REFERENCES

Achnine, L., Huhman, D.V., Farag, M.A., Sumner, L.W., Blount, J.W. and Dixon, R.A. (2005) Genomics-based selection and functional characterization of triterpene glycosyltransferases from the model legume *Medicago truncatula*. *Plant J.* **41**, 875–887.

Allen, M.B. and Arnon, D.I. (1955) Studies on nitrogen-fixing blue-green algae. I. Growth and nitrogen fixation by Anabaena cylindrica Lemm. *Plant Physiol.* **30**, 366–372.

Annesley, T.M. (2003) Ion suppression in mass spectrometry. *Clin. Chem.* **49**, 1041–1044.

Bacher, A., Eberhardt, S., Fischer, M., Kis, K. and Richter, G. (2000) Biosynthesis of vitamin B-2 (riboflavin). *Annu. Rev. Nutr.* **20**, 153–167.

Bais, H.P., Weir, T.L., Perry, L.G., Gilroy, S. and Vivanco, J.M. (2006) The role of root exudates in rhizosphere interations with plants and other organisms. *Annu. Rev. Plant Biol.* 233–266.

Baral, B., da Silva, J.A.T. and Izaguirre-Mayoral, M.L. (2016) Early signaling, synthesis, transport and metabolism of ureides. *J. Plant Physiol.* **193**, 97–109.

Barsch, A., Carvalho, H.G., Cullimore, J.V. and Niehaus, K. (2006) GC-MS based metabolite profiling implies three interdependent ways of ammonium assimilation in *Medicago truncatula* root nodules. *J. Biotechnol.* **127**, 79–83.

Benkeblia, N., Shinano, T. and Osaki, M. (2007) Metabolite profiling and assessment of metabolome compartmentation of soybean leaves using non-aqueous fractionation and GC-MS analysis. *Metabolomics*, **3**, 297–305.

Bilkey, J., Tata, A., McKee, T.D., Porcari, A.M., Bluemke, E., Woolman, M., Ventura, M., Eberlin, M.N. and Zarrine-Afsar, A. (2016) Variations in the abundance of lipid biomarker ions in mass spectrometry images correlate to tissue density. *Anal. Chem.* **88**, 12099–12107.

Bomsel, J.-L. and Pradet, A. (1968) Study of adenosine 5′-mono-, di-and triphosphates in plant tissues. IV. Regulation of the level of nucleotides, in vivo, by adenylate kinase: theoretical and experimental study. *Biochim. Biophys. Acta*, **162**, 230–242.

Borsdorf, H. and Eiceman, G.A. (2006) Ion mobility spectrometry: principles and applications. *Appl. Spectrosc. Rev.* **41**, 323–375.

Boughton, B.A., Thinagaran, D., Sarabia, D., Bacic, A. and Roessner, U. (2015) Mass spectrometry imaging for plant biology: a review. *Phytochem. Rev.* 1–44.

Brewin, N.J. (1991) Development of the legume root nodule. *Annu. Rev. Cell Biol.* **7**, 191–226.

Castro-Perez, J., Roddy, T.P., Nibbering, N.M.M. *et al.* (2011) Localization of fatty acyl and double bond positions in phosphatidylcholines using a dual stage CID fragmentation coupled with ion mobility mass spectrometry. *J. Am. Soc. Mass Spectrom.* **22**, 1552–1567.

Colebatch, G., Desbrosses, G., Ott, T., Krusell, L., Montanari, O., Kloska, S., Kopka, J. and Udvardi, M.K. (2004) Global changes in transcription orchestrate metabolic differentiation during symbiotic nitrogen fixation in Lotus japonicus. *Plant J.* **39**, 487–512.

Crawford, N.M. (1995) Nitrate – nutrient and signal for plant-growth. *Plant Cell*, **7**, 859–868.

Dettmer, K., Aronov, P.A. and Hammock, B.D. (2007) Mass spectrometry-based metabolomics. *Mass Spectrom. Rev.* **26**, 51–78.

Dixon, R.A. and Strack, D. (2003) Phytochemistry meets genome analysis, and beyond. *Phytochemistry*, **62**, 815–816.

van der Drift, K., Olsthoorn, M.M.A., Brull, L.P., Blok-Tip, L. and Thomas-Oates, J.E. (1998) Mass spectrometric analysis of lipo-chitin oligosaccharides – Signal molecules mediating the host-specific legume-rhizobium symbiosis. *Mass Spectrom. Rev.* **17**, 75–95.

Etalo, D.W., De Vos, R.C.H., Joosten, M.H.A.J. and Hall, R.D. (2015) Spatially resolved plant metabolomics: some potentials and limitations of Laser-Ablation electrospray ionization mass spectrometry metabolite imaging. *Plant Physiol.* **169**, 1424–1435.

Fiehn, O. (2002) Metabolomics – the link between genotypes and phenotypes. *Plant Mol. Biol.* **48**, 155–171.

Fiehn, O. (2006) Metabolite profiling in Arabidopsis. In *Arabidopsis Protocols* (Salinas, J. and SanchezSerrano, J.J., eds). Totowa, NJ: Humana Press, pp. 439–447.

Fiehn, O., Kopka, J., Dormann, P., Altmann, T., Trethewey, R.N. and Willmitzer, L. (2000) Metabolite profiling for plant functional genomics. *Nat. Biotechnol.* **18**, 1157–1161.

Field, B. and Osbourn, A.E. (2008) Metabolic diversification – Independent assembly of operon-like gene clusters in different plants. *Science*, **320**, 543–547.

Freiberg, C., Fellay, R., Bairoch, A., Broughton, W.J., Rosenthal, A. and Perret, X. (1997) Molecular basis of symbiosis between Rhizobium and legumes. *Nature*, **387**, 394–401.

Gaude, N., Tippmann, H., Flemetakis, E., Katinakis, P., Udvardi, M. and Dormann, P. (2004) The galactolipid digalactosyldiacylglycerol accumulates in the peribacteroid membrane of nitrogen-fixing nodules of soybean and Lotus. *J. Biol. Chem.* **279**, 34624–34630.

Gaye, M.M., Kurulugama, R. and Clemmer, D.E. (2015) Investigating carbohydrate isomers by IMS-CID-IMS-MS: precursor and fragment ion cross-sections. *Analyst*, **14**, 6922–6932.

Gemperline, E., Jayaraman, D., Maeda, J., Ane, J.-M. and Li, L. (2015) Multifaceted investigation of metabolites during nitrogen fixation in Medicago via high resolution MALDI-MS imaging and ESI-MS. *J. Am. Soc. Mass Spectrom.* **26**, 149–158.

Gemperline, E., Keller, C. and Li, L.J. (2016) Mass spectrometry in plant-omics. *Anal. Chem.* **88**, 3422–3434.

Gibson, S.I. (2000) Plant sugar-response pathways. Part of a complex regulatory web. *Plant Physiology*, **124**, 1532–1539.

Harada, K. and Fukusaki, E. (2009) Profiling of primary metabolite by means of capillary electrophoresis-mass spectrometry and its application for plant science. *Plant Biotechnol.* **26**, 47–52.

Kanu, A.B., Dwivedi, P., Tam, M., Matz, L. and Hill, H.H. Jr (2008) Ion mobility-mass spectrometry. *J. Mass Spectrom.* **43**, 1–22.

Kemen, A.C., Honkanen, S., Melton, R.E., Findlay, K.C., Mugford, S.T., Hayashi, K., Haralampidis, K., Rosser, S.J. and Osbourn, A. (2014) Investigation of triterpene synthesis and regulation in oats reveals a role for beta-amyrin in determining root epidermal cell patterning. *Proc. Natl Acad. Sci. USA*, **111**, 8679–8684.

Kiss, A., Smith, D.F., Reschke, B.R., Powell, M.J. and Heeren, R.M.A. (2014) Top-down mass spectrometry imaging of intact proteins by laser ablation ESIFT-ICR MS. *Proteomics*, **14**, 1283–1289.

Kitagawa, I., Taniyama, T., Nagahama, Y., Okubo, K., Yamauchi, F. and Yoshikawa, M. (1988) Saponin and sapogenol.42. structures of acetyl-soyasaponin-a1, acetyl-soyasaponin-a2, and acetyl-soyasaponin-a3, astringent partially acetylated bisdesmosides of soyasapogenol-a, from american soybean, the seeds of Glycine-max merrill. *Chem. Pharm. Bull. (Tokyo)*, **36**, 2819–2828.

Lardi, M., Murset, V., Fischer, H.-M., Mesa, S., Ahrens, C.H., Zamboni, N. and Pessi, G. (2016) Metabolomic profiling of bradyrhizobium diazoefficiens-induced root nodules reveals both host plant-specific and developmental signatures. *Int. J. Mol. Sci.* **17**, 815–834.

Li, H., Giles, K., Bendiak, B., Kaplan, K., Siems, W.F. and Hill, H.H. Jr (2012) Resolving structural isomers of monosaccharide methyl glycosides using drift tube and traveling wave ion mobility mass spectrometry. *Anal. Chem.* **84**, 3231–3239.

Li, H., Smith, B.K., Mark, L., Nemes, P., Nazarian, J. and Vertes, A. (2015) Ambient molecular imaging by laser ablation electrospray ionization mass spectrometry with ion mobility separation. *Int. J. Mass Spectrom.* **377**, 681–689.

Libault, M., Farmer, A., Brechenmacher, L. *et al.* (2010) Complete transcriptome of the soybean root hair cell, a single-cell model, and its alteration in response to *Bradyrhizobium japonicum* infection. *Plant Physiol.* **152**, 541–552.

May, J.C., Goodwin, C.R. and McLean, J.A. (2015) Ion mobility-mass spectrometry strategies for untargeted systems, synthetic, and chemical biology. *Curr. Opin. Biotechnol.* **31**, 117–121.

McCormick, D.B. (1989) 2 Interconnected vitamin-b – riboflavin and pyridoxine. *Physiol. Rev.* **69**, 1170–1198.

Mueller, T., Oradu, S., Ifa, D.R., Cooks, R.G. and Kraeutler, B. (2011) Direct plant tissue analysis and imprint imaging by desorption electrospray ionization mass spectrometry. *Anal. Chem.* **83**, 5754–5761.

Murray, J.D., Karas, B.J., Sato, S., Tabata, S., Amyot, L. and Szczyglowski, K. (2007) A cytokinin perception mutant colonized by Rhizobium in the absence of nodule organogenesis. *Science*, **315**, 101–104.

Nadler, K.D. and Avissar, Y.J. (1977) Heme synthesis in soybean root-nodules. 1. Role of bacteroid delta-aminolevulinic-acid synthase and delta-aminolevulinic-acid dehydrase in synthesis of heme of leghemoglobin. *Plant Physiol.* **60**, 433–436.

Nemes, P. and Vertes, A. (2007) Laser ablation electrospray ionization for atmospheric pressure, in vivo, and imaging mass spectrometry. *Anal. Chem.* **79**, 8098–8106.

Nemes, P., Huang, H.H. and Vertes, A. (2012) Internal energy deposition and ion fragmentation in atmospheric-pressure mid-infrared laser ablation electrospray ionization. *PCCP*, **14**, 2501–2507.

Oldroyd, G.E.D. and Downie, J.M. (2008) Coordinating nodule morphogenesis with rhizobial infection in legumes. *Annu. Rev. Plant Biol.* 519–546.

Oliveira, A.L.M., Urquiaga, S., Dobereiner, J. and Baldani, J.I. (2002) The effect of inoculating endophytic N-2-fixing bacteria on micropropagated sugarcane plants. *Plant Soil*, **242**, 205–215.

Oms-Oliu, G., Hertog, M., Van de Poel, B., Ampofo-Asiama, J., Geeraerd, A.H. and Nicolai, B.M. (2011) Metabolic characterization of tomato fruit during preharvest development, ripening, and postharvest shelf-life. *Postharvest Biol. Technol.* **62**, 7–16.

Paglia, G., Williams, J.P., Menikarachchi, L. *et al.* (2014) Ion mobility derived collision cross sections to support metabolomics applications. *Anal. Chem.* **86**, 3985–3993.

Pu, L. and Brady, S. (2010) Systems biology update: cell type-specific transcriptional regulatory networks. *Plant Physiol.* **152**, 411–419.

Rolfe, B.G. (1988) Flavones and isoflavones as inducing substances of legume nodulation. *BioFactors*, **1**, 3–10.

Schauer, N., Semel, Y., Roessner, U. *et al.* (2006) Comprehensive metabolic profiling and phenotyping of interspecific introgression lines for tomato improvement. *Nat. Biotechnol.* **24**, 447–454.

Schliemann, W., Ammer, C. and Strack, D. (2008) Metabolite profiling of mycorrhizal roots of *Medicago truncatula*. *Phytochemistry*, **69**, 112–146.

Schmidt, H., Gunther, C., Weber, M., Sporlein, C., Loscher, S., Bottcher, C., Schobert, R. and Clemens, S. (2014) Metabolome analysis of *Arabidopsis thaliana* roots identifies a key metabolic pathway for iron acquisition. *PLoS ONE*, **9**, e102444.

Schubert, K.R. (1986) Products of biological nitrogen-fixation in higher-plants – synthesis, transport, and metabolism. *Annu. Rev. Plant Physiol. Plant Mol. Biol.* **37**, 539–574.

Schwinghamer, E.A. (1970) Requirement for riboflavin for effective symbiosis on clover by an auxotrophic mutant strain of rhizobium-trifolii. *Aust. J. Biol. Sci.* **23**, 1187–1196.

Shaw, J.B., Lin, T.Y., Leach, F.E. 3rd, Tolmachev, A.V., Tolic, N., Robinson, E.W., Koppenaal, D.W. and Pasa-Tolic, L. (2016) 21 Tesla Fourier transform ion cyclotron resonance mass spectrometer greatly expands mass spectrometry toolbox. *J. Am. Soc. Mass Spectrom.* **27**, 1929–1936.

Shrestha, B. and Vertes, A. (2014) High-throughput cell and tissue analysis with enhanced molecular coverage by laser ablation electrospray ionization mass spectrometry using ion mobility separation. *Anal. Chem.* **86**, 4308–4315.

Shvartsburg, A.A. and Smith, R.D. (2008) Fundamentals of traveling wave ion mobility spectrometry. *Anal. Chem.* **80**, 9689–9699.

Smith, P.M.C. and Atkins, C.A. (2002) Purine biosynthesis. Big in cell division, even bigger in nitrogen assimilation. *Plant Physiol.* **128**, 793–802.

Sparg, S.G., Light, M.E. and van Staden, J. (2004) Biological activities and distribution of plant saponins. *J. Ethnopharmacol.* **94**, 219–243.

Stacey, G. (2007) The rhizobium-legume nitrogen-fixing symbiosis. In *Biology of the Nitrogen Cycle*, (Bothe, H., Ferguson, S.J. and Newton, W.E., eds), Chapter 10, Amsterdam: Elsevier, pp. 147–163.

Stacey, G., Libault, M., Brechenmacher, L., Wan, J.R. and May, G.D. (2006) Genetics and functional genomics of legume nodulation. *Curr. Opin. Plant Biol.* **9**, 110–121.

Stopka, S.A., Shrestha, B., Marechal, E., Falconet, D. and Vertes, A. (2014) Metabolic transformation of microalgae due to light acclimation and genetic modifications followed by laser ablation electrospray ionization mass spectrometry with ion mobility separation. *Analyst*, **139**, 5945–5953.

Stopka, S.A., Mansour, T.R., Shrestha, B., Marechal, E., Falconet, D. and Vertes, A. (2016) Turnover rates in microorganisms by laser ablation electrospray ionization mass spectrometry and pulse-chase analysis. *Anal. Chim. Acta*, **902**, 1–7.

Strohalm, M., Hassman, M., Kosata, B. and Kodicek, M. (2008) mMass data miner: an open source alternative for mass spectrometric data analysis. *Rapid Commun. Mass Spectrom.* **22**, 905–908.

Subramanian, S., Stacey, G. and Yu, O. (2007) Distinct, crucial roles of flavonoids during legume nodulation. *Trends Plant Sci.* **12**, 282–285.

Sulieman, S. (2011) Does GABA increase the efficiency of symbiotic N_2 fixation in legumes? *Plant Signal. Behav.* **6**, 32–36.

Sumner, L.W., Amberg, A., Barrett, D. *et al.* (2007) Proposed minimum reporting standards for chemical analysis. *Metabolomics*, **3**, 211–221.

Thimmappa, R., Geisler, K., Louveau, T., O'Maille, P. and Osbourn, A. (2014) Triterpene biosynthesis in plants. *Annu. Rev. Plant Biol.* **65**, 225–257.

Upchurch, R.G. and Mortenson, L.E. (1980) Invivo energetics and control of nitrogen-fixation – changes in the adenylate energy-charge and adenosine 5′-diphosphate – adenosine 5′-triphosphate ratio of cells during growth on dinitrogen versus growth on ammonia. *J. Bacteriol.* **143**, 274–284.

Vanrhijn, P. and Vanderleyden, J. (1995) The rhizobium-plant symbiosis. *Microbiol. Rev.* **59**, 124–142.

Vauclare, P., Bligny, R., Gout, E. and Widmer, F. (2013) An overview of the metabolic differences between Bradyrhizobium japonicum 110 bacteria and differentiated bacteroids from soybean (Glycine max) root nodules: an in vitro 13C-and 31P-nuclear magnetic resonance spectroscopy study. *Fems Microbiology Letters*, **343**, 49–56.

Vincken, J.-P., Heng, L., de Groot, A. and Gruppen, H. (2007) Saponins, classification and occurrence in the plant kingdom. *Phytochemistry*, **68**, 275–297.

Wang, J., Si, Z., Li, F., Xiong, X., Lei, L., Xie, F., Chen, D., Li, Y. and Li, Y. (2015) A purple acid phosphatase plays a role in nodule formation and nitrogen fixation in *Astragalus sinicus*. *Plant Mol. Biol.* **88**, 515–529.

Weckwerth, W. (2003) Metabolomics in systems biology. *Annu. Rev. Plant Biol.* **54**, 669–689.

White, J., Prell, J., James, E.K. and Poole, P. (2007) Nutrient sharing between symbionts. *Plant Physiol.* **144**, 604–614.

Wyttenbach, T., Pierson, N.A., Clemmer, D.E. and Bowers, M.T. (2014) Ion mobility analysis of molecular dynamics. *Annu. Rev. Phys. Chem.*, **65**, 175–196.

Yang, G.P., Bhuvaneswari, T.V., Joseph, C.M., King, M.D. and Phillips, D.A. (2002) Roles for riboflavin in the Sinorhizobium – Alfalfa association. *Mol. Plant Microbe Interact.* **15**, 456–462.

Ye, H., Gemperline, E., Venkateshwaran, M., Chen, R., Delaux, P.-M., Howes-Podoll, M., Ane, J.-M. and Li, L. (2013) MALDI mass spectrometry-assisted molecular imaging of metabolites during nitrogen fixation in the *Medicago truncatula-Sinorhizobium meliloti* symbiosis. *Plant J.* **75**, 130–145.

Yurgel, S.N., Rice, J., Domreis, E., Lynch, J., Sa, N., Qamar, Z., Rajamani, S., Gao, M., Roje, S. and Bauer, W.D. (2014) *Sinorhizobium meliloti* flavin secretion and bacteria-host interaction: role of the bifunctional RibBA protein. *Mol. Plant Microbe Interact.* **27**, 437–445.

Zahran, H.H. (1999) Rhizobium-legume symbiosis and nitrogen fixation under severe conditions and in an arid climate. *Microbiol. Mol. Biol. Rev.* **63**, 968–+.

Zhang, J.Y., de Carvalho, M.H.C., Torres-Jerez, I., Kang, Y., Allen, S.N., Huhman, D.V., Tang, Y.H., Murray, J., Sumner, L.W. and Udvardi, M.K. (2014) Global reprogramming of transcription and metabolism in *Medicago truncatula* during progressive drought and after rewatering. *Plant, Cell Environ.* **37**, 2553–2576.

Zhuang, X.L., Gao, J., Ma, A.Z., Fu, S.L. and Zhuang, G.Q. (2013) Bioactive molecules in soil ecosystems: masters of the underground. *Int. J. Mol. Sci.* **14**, 8841–8868.

Zrenner, R., Stitt, M., Sonnewald, U. and Boldt, R. (2006) Pyrimidine and purine biosynthesis and degradation in plants. *Annu. Rev. Plant Biol.* **57**, 805–836.

Laser Ablation Electrospray Ionization Mass Spectrometry with Ion Mobility Separation Reveals Metabolites in the Symbiotic Interactions of Soybean Roots and Rhizobia

Supporting Information

Sylwia A. Stopka,[1] Beverly J. Agtuca,[2] David W. Koppenaal,[3] Ljiljana Paša-Tolić,[3] Gary Stacey,[2] Akos Vertes,[1] and Christopher R. Anderton[3*]

[1]Department of Chemistry, W. M. Keck Institute for Proteomics Technology and Applications, The George Washington University, Washington, DC 20052; [2]Divisions of Plant Sciences and Biochemistry, C. S. Bond Life Sciences Center, University of Missouri, Columbia, MO 65211; [3]Environmental Molecular Sciences Laboratory, Earth and Biological Sciences Directorate, Pacific Northwest National Laboratory, 902 Battelle Boulevard, Richland, Washington 99354

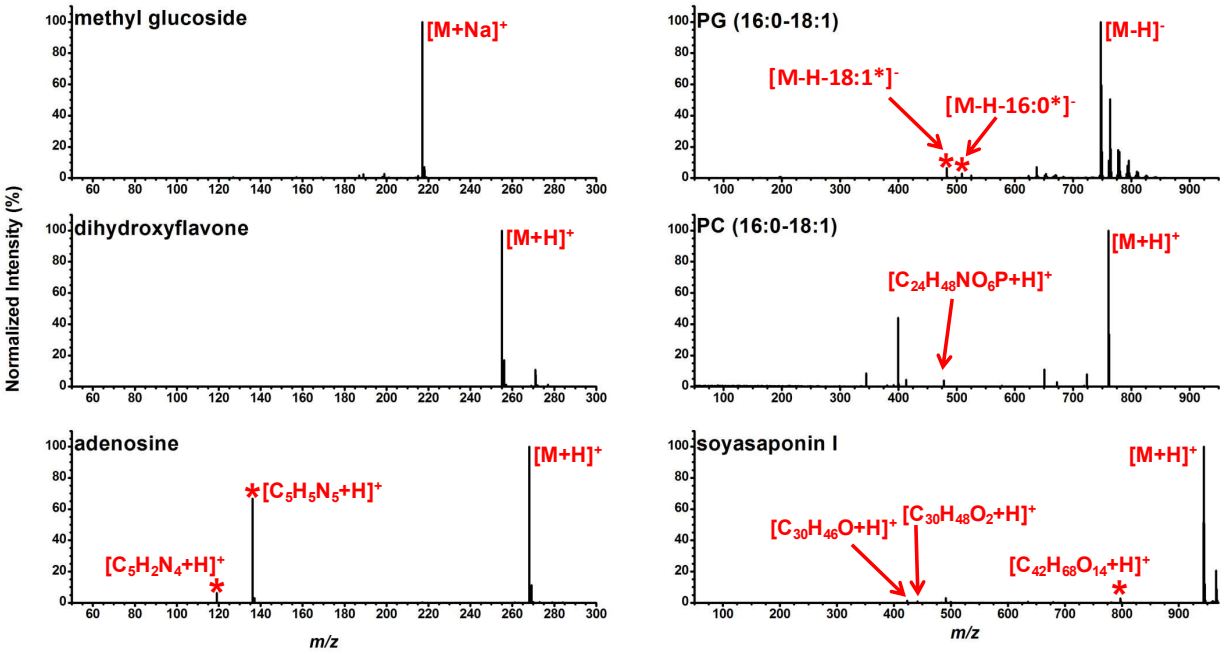

Figure S1. LAESI-MS analysis of standards, which were selected based on their presence within the intact soybean nodules, illustrates the extent of in-source fragmentation of these metabolites. Adenosine exhibited a 61.4% fragmentation from the observed parent peak to adenine from the LAESI process, as compared to 37.4% in-source fragmentation from ESI alone—therefore, 24.0% of the fragmentation is induced by the laser ablation process. Other compounds showed no parent ion decay (e.g., the glucoside and flavone). The extent of lipid decomposition due to the LAESI-MS technique revealed that in-source fragmentation of lipid species did not yield fatty acid ions, but rather the corresponding ketene cleavage products for the PG and PC species. Furthermore, there was no observed phosphocholine head group from the PC species. (*) Represents unique ions produced during LAESI-MS in-source fragmentation as opposed to ESI alone.

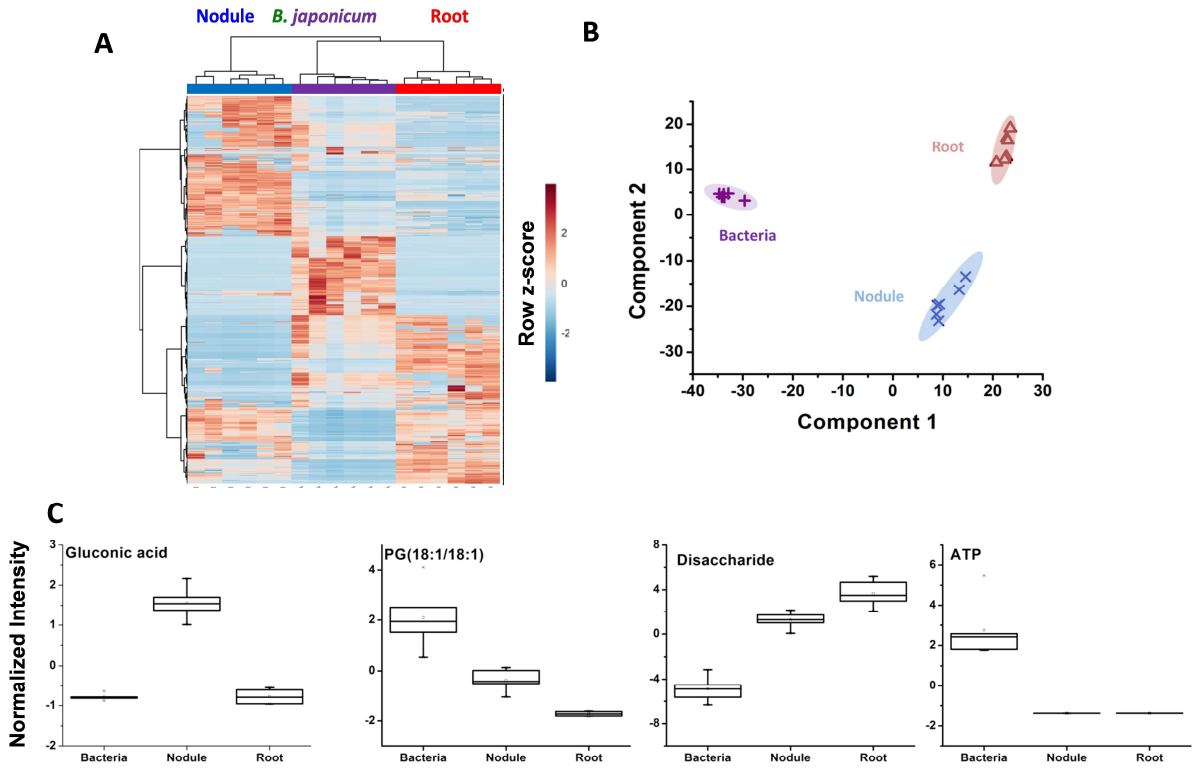

Figure S2. Corresponding negative ion mode data to Figure 3. (A) Heat-map illustrating the major spectral difference based on normalized negative ion spectra, where each column is a spectrum and each row is an *m/z*. The color for the samples of the heat map represents the relative abundance of metabolites: red is greater relative abundance and blue is lower relative abundance. (B) Scores plot from PLS-DA of the spectra, which were used to assist in identifying minor species that are significant in each system with a 95% confidence. The corresponding loadings plots from PLS-DA of the spectra were used to identify peaks of interest. (C) Relative abundances of four significant species as identified from the loadings plots.

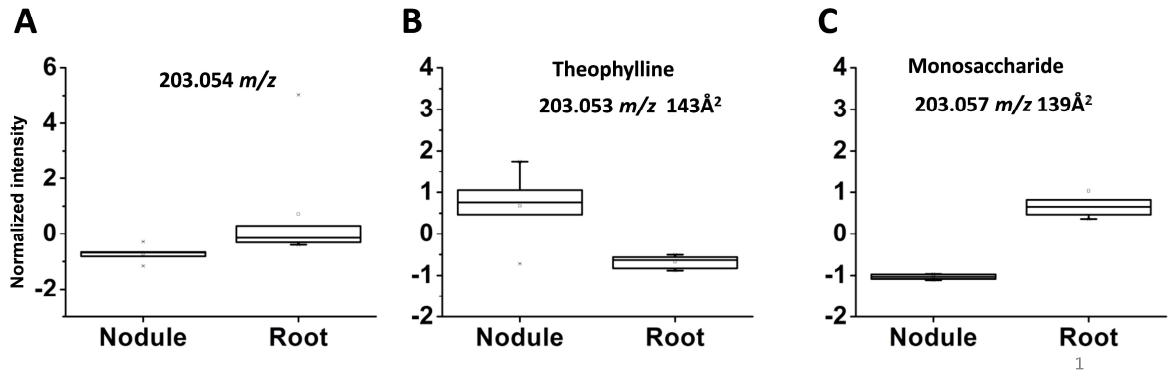

Figure S3. Demonstrating the utility of IMS in resolving isobaric species. (A) Box-and-whisker plot of the relative abundance of the *m/z* 203.054 in the root nodule and uninfected root without IMS, where there is no significant difference in the root nodule and uninfected root samples. Implementation of IMS showed two isobaric ions at the nominal mass of *m/z* 203 that were separated based on their unique CCS values. Based on tentative assignments, we see (B) theophylline in more abundant in the nodule and (C) monosaccharide is significantly more present in the uninfected root sample.

Laser Ablation Electrospray Ionization Mass Spectrometry with Ion Mobility Separation Reveals Metabolites in the Symbiotic Interactions of Soybean Roots and Rhizobia

Supporting Information

Sylwia A. Stopka,[1] Beverly J. Agtuca,[2] David W. Koppenaal,[3] Ljiljana Paša-Tolić,[3] Gary Stacey,[2] Akos Vertes,[1] and Christopher R. Anderton[3*]

[1]Department of Chemistry, W. M. Keck Institute for Proteomics Technology and Applications, The George Washington University, Washington, DC 20052; [2]Divisions of Plant Sciences and Biochemistry, C. S. Bond Life Sciences Center, University of Missouri, Columbia, MO 65211; [3]Environmental Molecular Sciences Laboratory, Earth and Biological Sciences Directorate, Pacific Northwest National Laboratory, 902 Battelle Boulevard, Richland, Washington 99354

Table S1. Relative abundances of the chemical species detected from free-living rhizobia, root nodules, and uninfected root segments with tentative assignments based on the observed *m/z*, tandem MS, collision cross sections, and Metabolomics Standard Initiative (MSI) level of metabolite identification (Sumner et al., 2007).

	Compound	Kegg	Bacteria (%)	Nodule (%)	Root (%)	Ion	Formula	Meas. Mass	Δm (mDa)	CCS Meas. (Å²)	CCS ref (Å²)	ΔCCS (Å²)	MSI level
Sugars and polysaccharides	**Monosaccharide**	C00216		16.0	14.7	$[M-H]^-$	$C_5H_{10}O_5$	149.045	-1.0	120			3
	Monosaccharide[a]	C00095		2.6	2.5	$[M-H]^-$	$C_6H_{12}O_6$	179.056	0.1	127			2
	Monosaccharide[a]	C00095		3.2	2.2	$[M+Na]^+$	$C_6H_{12}O_6$	203.051	-1.6	139	138*	1	1
	Disaccharide[a]	C00089	13.3	97.5	91.8	$[M-H]^-$	$C_{12}H_{22}O_{11}$	341.115	7.0	166	165*	1	1
	Disaccharide[a]	C00089	31.2	54.5	99.8	$[M+Na]^+$	$C_{12}H_{22}O_{11}$	365.106	0.4	188	185*	2	1
	Disaccharide[a]	C00089	16.4	100	100	$[M+K]^+$	$C_{12}H_{22}O_{11}$	381.079	-0.8	183	182*	1	1
	Trisaccharide	C01835	3.2	1.8	2.6	$[M+Na]^+$	$C_{18}H_{32}O_{16}$	527.157	-1.4	209	212*	-3	3
	Trisaccharide	C01835		4.3	3.5	$[M+K]^+$	$C_{18}H_{32}O_{16}$	543.136	3.8	211			3
Amino acids	**Citrulline**	C00327	1.3	4.4	1.2	$[M+Na]^+$	$C_6H_{13}N_3O_3$	198.084	-0.8	142	141*	1	3
	Arginine[a]	C00062	12.8			$[M+H]^+$	$C_6H_{14}N_4O_2$	175.121	2.0	135	133*	2	1
	Glutamine	C00064		1.1		$[M-H]^-$	$C_5H_{10}N_2O_3$	145.060	-2.2	127	126*	1	3
	Glutamate	C00025	1.8	4.1		$[M-H]^-$	$C_5H_9NO_4$	146.049	2.8	120	123*	-3	3
Organic acids	**Malic acid**	C00149		1.9	1.3	$[M-H]^-$	$C_4H_6O_5$	133.010	-4.0	115	117[c]	-2	3
	Phosphoenolpyruvic acid	C00074		1.3	1.1	$[M-H]^-$	$C_3H_5O_6P$	166.977	2.6				3
	Vanillic acid[b]	C06672		2.9	3.0	$[M-H]^-$	$C_8H_8O_4$	167.034	-0.9	127			2
	Gluconic acid	C00257		15.9	8.4	$[M-H]^-$	$C_6H_{12}O_7$	195.051	0.4	130	131*	-1	3
	Azelaic acid	C08261		7.6		$[M-H]^-$	$C_9H_{16}O_4$	187.097	-0.5	136	134*	2	3
	Azelaic acid	C08261		1.1		$[M+Na]^+$	$C_9H_{16}O_4$	211.092	1.8	152	148*	4	3
	Arachidic acid[a]	C06425		79.9	41.5	$[M-H]^-$	$C_{20}H_{40}O_2$	311.297	1.3	183	186*	-3	1
Fatty acids	**Jasmonic acid**	C08491		11.1	4.4	$[M-H]^-$	$C_{12}H_{18}O_3$	209.118	0.1	148			3
	Palmitic acid[a]	C00249		1.8		$[M-H]^-$	$C_{16}H_{32}O_2$	255.234	0.7	168	170*	-2	1

	Linoleic acid	C01595		9.2		[M-H]$^-$	$C_{18}H_{32}O_2$	279.230	-3.1	175			3
	Oleic acid	C00712		12.2		[M-H]$^-$	$C_{18}H_{34}O_2$	281.248	-0.9	176	176*	0	3
	Stearic acid[b]	C01530		29.1		[M-H]$^-$	$C_{18}H_{36}O_2$	283.265	1.1	179			2
Growth Factors	**Choline**[b]	C00114		2.14	3.0	[M+H]$^+$	$C_5H_{13}NO$	104.110	3.0	122	117[c]	5	2
	Riboflavin	C00255		2.4		[M+H]$^+$	$C_{17}H_{20}N_4O_6$	377.153	2.9	171	171*	0	3
	Niacinamide	C00153		2.1		[M+H]$^+$	$C_6H_6N_2O$	123.058	2.3	120	122*	-2	3
	Isopentenyladenine	C04083		48.5		[M+H]$^+$	$C_{10}H_{13}N_5$	204.125	0.5	148	145*	3	3
Nucleotides	**Adenine**[a]	C00147	5.9	12.8		[M-H]$^-$	$C_5H_5N_5$	134.049	1.7	112	114*	-2	1
	Adenine[a]	C00147	7.1	14.9	1.1	[M+H]$^+$	$C_5H_5N_5$	136.062	0.6	121	120*	1	3
	Guanine	C00242	2.4	1.1	1.8	[M+H]$^+$	$C_5H_5N_5O$	152.052	-4.5	120	124[c]	-4	3
	Adenosine[b]	C00212	1.4	1.5	1.4	[M+H]$^+$	$C_{10}H_{13}N_5O_4$	268.104	-0.3	155	151[c]	4	3
Flavonones	**Dihydroxyflavone**[b]	C14344		86.6	100	[M-H]$^-$	$C_{15}H_{10}O_4$	253.052	0.9	153			2
	Dihydroxyflavone[b]	C14344		43.8	60.4	[M+H]$^+$	$C_{15}H_{10}O_4$	255.063	-2.2	170			2
	Hydroxy methoxyisoflavone			6.6	5.4	[M-H]$^-$	$C_{16}H_{12}O_4$	267.073	6.2	148			3
				1.3	1.6	[M+Na]$^+$	$C_{16}H_{12}O_4$	309.039	2.0				3
	Trihydroxyflavone[a]	C06563		39.2	53.4	[M-H]$^-$	$C_{15}H_{10}O_5$	269.045	-1.0	153	151*	2	1
	Trihydroxyflavone[a]	C06563		3.7	9.2	[M+H]$^+$	$C_{15}H_{10}O_5$	271.063	2.5	160	157*	3	1
	Dihydroxy methoxyflavone[a]			2.8	3.5	[M+H]$^+$	$C_{16}H_{12}O_5$	285.071	-5.9	157	159*	-3	1
	Tetrahydroxyflavone			2.6	5.8	[M-H]$^-$	$C_{15}H_{10}O_6$	285.044	3.5	154			3
	Dihydroxy dimethoxyisoflavanone[a]			6.2	9.5	[M-H]$^-$	$C_{17}H_{16}O_6$	315.082	-5.0	156	160*	-4	1
	Tetramethoxyflavanone			3.1	6.5	[M-H]$^-$	$C_{19}H_{20}O_6$	343.120	1.0	165			3
	Dihydroxy tetramethoxy methylenedioxy flavone			4.3	24.3	[M-H]$^-$	$C_{20}H_{18}O_{10}$	417.079	-3.4	174			3
	Tetramethoxy methylenedioxy flavone			1.9	21.5	[M-H]$^-$	$C_{21}H_{18}O_{10}$	429.078	-4.6	187			3

Glucosides	**methyl glucoside**	C03619		4.6	1.6	$[M-H]^-$	$C_7H_{14}O_6$	193.076	4.8	133			3
	Tuberonic acid glucoside	C08558		18.8		$[M-H]^-$	$C_{18}H_{28}O_9$	387.162	-4.0	172			3
	Trihydroxyflavone glucoside	C01460		28.1	10.9	$[M-H]^-$	$C_{21}H_{20}O_{10}$	431.095	-3.7	206			3
	Trihydroxyflavanone glucoside[b]	C09099		8.8	12.6	$[M-H]^-$	$C_{21}H_{22}O_{10}$	433.111	-3.5	199			2
	Dihydroxy methoxyflavone glucoside	C10381		7.8	4.32	$[M-H]^-$	$C_{22}H_{22}O_{10}$	445.120	6.1	189			3
	Tetrahydroxyflavone glucoside[b]			9.1	21.3	$[M+Na]^+$	$C_{21}H_{20}O_{11}$	471.093	3.2				2
	Tetrahydroxyflavanone glucoside[b]			8.2	2.9	$[M-H]^-$	$C_{21}H_{22}O_{11}$	449.105	-3.6	197			2
	Hydroxy dimethoxyflavone glucoside			9.5		$[M-H]^-$	$C_{23}H_{24}O_{10}$	459.126	-3.4	201			3
	Dihydroxy dimethoxyisoflavone glucoside			20.0	7.5	$[M-H]^-$	$C_{23}H_{24}O_{11}$	475.121	-4.1	205			3
	Flavonol malonyl glucoside			12.8	x	$[M-H]^-$	$C_{24}H_{22}O_{11}$	485.104	-4.5	193			3
	Trihydroxy trimethoxyflavone glucoside			6.1		$[M-H]^-$	$C_{24}H_{26}O_{13}$	521.126	-4.5	217			3
	Trihydroxy trimethoxyflavone glucuronide				1.2	$[M-H]^-$	$C_{24}H_{24}O_{14}$	535.107	-2.4	219			3
	Tetrahydroxy tetramethoxyflavone glucoside[b]			10.2		$[M-H]^-$	$C_{25}H_{28}O_{15}$	567.145	9.7	223			2
Lipids	**PA (18:2/18:2)[b]**			34.4	2.3	$[M-H]^-$	$C_{39}H_{69}O_8P$	695.464	-1.9	214			2
	PE (16:1/18:1)[b]	C00350	12.8	9.4		$[M-H]^-$	$C_{39}H_{74}NO_8P$	714.506	-2.3	274			2
	PE (16:0/18:1)[b]		23.6	5.4		$[M-H]^-$	$C_{39}H_{76}NO_8P$	716.516	-7.8	282			2
	PG (16:0/18:1)[b]		34.9	17.6		$[M-H]^-$	$C_{40}H_{77}O_{10}P$	747.521	3.2	287			2
	PG (18:1/18:1)[b]		12.7	22.2		$[M-H]^-$	$C_{42}H_{79}O_{10}P$	773.535	0.7	315			2
Triterpenes	**Soyasaponin II[b]**	C12081		34.9	26.6	$[M-H]^-$	$C_{47}H_{76}O_{17}$	911.501	-0.1	330			2
	Soyasaponin II[b]	C12081		5.4	1.1	$[M+H]^+$	$C_{47}H_{76}O_{17}$	913.521	6.0	313			2
	Dehydrosoyasaponin I[b]	C13837		10.0	7.2	$[M-H]^-$	$C_{48}H_{76}O_{18}$	939.495	-1.0	325			2
	Dehydrosoyasaponin I[b]	C13837		3.6	1.3	$[M+H]^+$	$C_{48}H_{76}O_{18}$	941.521	10.6	331			2

	Soyasaponin I[b]	C08983		52.5	46.2	$[M-H]^-$	$C_{48}H_{78}O_{18}$	941.517	5.7	331			2
	Soyasaponin I[b]	C08983		4.5	1.6	$[M+H]^+$	$C_{48}H_{78}O_{18}$	943.527	0.9	328			2
	Soyasaponin V[b]			4.3	9.2	$[M-H]^-$	$C_{48}H_{78}O_{19}$	957.505	-2.0	334			2
	Soyasaponin V[b]			1.9	1.8	$[M+H]^+$	$C_{48}H_{78}O_{19}$	959.530	9.4	357			2
	Soyasaponin aa[b]			10.7	1.4	$[M-H]^-$	$C_{53}H_{82}O_{21}$	1053.525	-2.8	362			2
	Soyasaponin aa[b]			3.16	1.5	$[M+H]^+$	$C_{53}H_{82}O_{21}$	1055.539	-5.9	365			2
	Soyasaponin bg[b]			3.11	2.3	$[M-H]^-$	$C_{54}H_{84}O_{21}$	1067.548	4.9	368			2
	Soyasaponin bg[b]			18.0	1.2	$[M+H]^+$	$C_{54}H_{84}O_{21}$	1069.551	-7.3	367			2
	Soyasaponin ag[b]			19.5	3.7	$[M-H]^-$	$C_{54}H_{84}O_{22}$	1083.536	-1.7	372			2
	Soyasaponin ag[b]			4.5	1.1	$[M+H]^+$	$C_{54}H_{84}O_{22}$	1085.546	-7.2	370			2
Others	**cyclohexylammonium[b]**	C00571		2.1	1.7	$[M+H]^+$	$C_6H_{13}N$	100.114	1.9	123			2
	Uridine diphosphate acetylglucosamine[a]	C00043	4.4			$[M-H]^-$	$C_{17}H_{27}N_3O_{17}P_2$	606.078	3.7	225	222*	3	1
	Methylmalonic	C02170	3.1	2.6		$[M+H]^+$	$C_4H_6O_4$	119.029	-1.3	127	125*	2	3
	Spermidine[a]	C00315		1.3	1.8	$[M+H]^+$	$C_7H_{19}N_3$	146.170	4.5	136	135*	1	1
	Allantoin	C01551	15.1	4.39		$[M+H]^+$	$C_4H_6N_4O_3$	159.056	5.0	183			3
	Theophylline	C07130		5.9		$[M-H]^-$	$C_7H_8N_4O_2$	179.051	-6.4	127	128*	-1	3
	Theophylline	C07130		1.7		$[M-H_2O-H]^-$	$C_7H_8N_4O_2$	161.050	3.7	125	128*	-2	3
	Theophylline	C07130		2.3		$[M+Na]^+$	$C_7H_8N_4O_2$	203.055	0.0	143	140*	3	3
	Phosphocholine	C00588		2.9		$[M+H]^+$	$C_5H_{14}NO_4P$	184.075	1.9	135	135*	0	3
	Acetyl glutamic acid	C00624		1.2		$[M+H]^+$	$C_7H_{11}NO_5$	188.058	1.6	132			2
	Glucose phosphate	C00668		14.9	3.7	$[M-H]^-$	$C_6H_{13}O_9P$	259.021	-1.7	143	142*	1	3
	Inosine	C00294	2.2	6.5	5.4	$[M-H]^-$	$C_{10}H_{12}N_4O_5$	267.073	-0.1	151			3
	Glycerol Phosphocholine			5.8	2.2	$[M+Na]^+$	$C_8H_{20}NO_6P$	280.098	8.0	162	160*	2	3
	Reduced glutathione[a]	C00051	79.0	10.4		$[M-H]^-$	$C_{10}H_{17}N_3O_6S$	306.073	-3.9	158	159*	-1	1

Reduced glutathione[a]	C00051	23.5			$[M+H]^+$	$C_{10}H_{17}N_3O_6S$	308.093	1.5	169	165*	4	1
Cytidine monophosphate	C00055	1.3			$[M-H]^-$	$C_9H_{14}N_3O_8P$	322.045	0.7	164	165*	-1	3
Uridine Monophosphate[a]	C00105	2.4	2.5	2.6	$[M+H]^+$	$C_9H_{13}N_2O_9P$	325.031	-9.0	162	164*	-2	1
Ajmaline	C06542		31.5	11.5	$[M-H]^-$	$C_{20}H_{26}N_2O_2$	325.201	8.9	166			3
jasmonoyl aminocyclopropane carboxylate			12.9		$[M+K]^+$	$C_{16}H_{23}NO4$	332.121	-5.9	151			3
Fructose Biphosphate	C06193	1.7			$[M-H]^-$	$C_6H_{14}O_{12}P_2$	338.996	8.1	164	165*	-1	3
Adenosine monophosphate[a]	C00020	4.9			$[M-H]^-$	$C_{10}H_{14}N_5O_7P$	346.064	7.8	163	165*	-2	1
Guanosine phosphate	C06193	1.7			$[M-H]^-$	$C_{10}H_{14}N_5O_8P$	362.061	10.8	177	178*	-2	3
Adenosylmethionine[a]	C00019	x	2.1		$[M+H]^+$	$C_{15}H_{22}N_6O_5S$	399.142	-2.4	167	169*	-2	1
Uridine Diphosphate	C00015	10.0			$[M-H]^-$	$C_9H_{14}N_2O_{12}P_2$	402.992	-2.9	177	182*	-5	3
Uridine Diphosphate	C00015	1.6			$[M+H]^+$	$C_9H_{14}N_2O_{12}P_2$	405.014	3.5	179	180*	-1	3
Adenosine Diphosphate[a]	C00008	42.5			$[M-H]^-$	$C_{10}H_{15}N_5O_{10}P_2$	426.026	4.5	179	180*	-1	1
Soyasapogenol E	C17420		37.8	48.5	$[M-H]^-$	$C_{30}H_{48}O_3$	455.349	-4.0	179			3
Adenosine triphosphate[a]	C00002	17.8			$[M-H]^-$	$C_{10}H_{16}N_5O_{13}P_3$	505.991	2.5	190	186*	4	1
Cyclic-ADP ribose[b]	C13050	28.1			$[M-H]^-$	$C_{15}H_{21}N_5O_{13}P_2$	540.054	3.0	226			2
Heme B[b]	C00032	2.3	11.5		Cation	$C_{34}H_{32}FeN_4O_4$	616.179	1.5	266			2

[a]Chemical species assigned by in-house reference standard MSMS performed under identical conditions

[b]Chemical species assigned by external standard MSMS databases comparison

[*]Chemical species CCS value obtained from our in-house CCS LAESI-IMS-MS library

[c]Chemical species CCS value obtained from literature (paglia 2014)

Laser Ablation Electrospray Ionization Mass Spectrometry with Ion Mobility Separation Reveals Metabolites in the Symbiotic Interactions of Soybean Roots and Rhizobia

Supporting Information

Sylwia A. Stopka,[1] Beverly J. Agtuca,[2] David W. Koppenaal,[3] Ljiljana Paša-Tolić,[3] Gary Stacey,[2] Akos Vertes,[1] and Christopher R. Anderton[3*]

[1]Department of Chemistry, W. M. Keck Institute for Proteomics Technology and Applications, The George Washington University, Washington, DC 20052; [2]Divisions of Plant Sciences and Biochemistry, C. S. Bond Life Sciences Center, University of Missouri, Columbia, MO 65211; [3]Environmental Molecular Sciences Laboratory, Earth and Biological Sciences Directorate, Pacific Northwest National Laboratory, 902 Battelle Boulevard, Richland, Washington 99354

EXPERIMENTAL PROCEDURES (continued)

Cell Culture and Plant Growth

Bradyrhizobium japonicum USDA110 cells were inoculated into HM medium (Cole and Elkan, 1973) (HEPES, 1.3 g L^{-1}; MES, 1.1 g L^{-1}; Na_2HPO_4, 0.125 g L^{-1}; Na_2SO_4, 0.25 g L^{-1}; NH_4Cl, 0.32 g L^{-1}; $MgSO_4 \cdot 7H_2O$, 0.18 g L^{-1}; $FeCl_3$, 0.004 g L^{-1}; $CaCl_2 \cdot 2H_2O$, 0.013 g L^{-1}; yeast extract, 0.25 g L^{-1}; D-Ara, 1 g L^{-1}; sodium gluconate, 1 g L^{-1}; and pH 6.6). The medium was supplemented with 25 mg/L of tetracycline and 100 mg/L of spectinomycin. The culture was incubated and maintained for 2 d at 30 °C in an orbital shaker (MaxQ400, Thermo Scientific, Waltham, MA) set to 180 rpm. Cellular growth was monitored by measuring optical density, and when the bacterial culture reached OD_{600}= 0.8 (10^8 cells/mL), the culture was centrifuged at 800 × g for 10 min, washed three times with DI water, and used for seedling inoculation.

Soybean seeds (*Glycine max* Williams 82) were first sterilized with 20% (v/v) bleach for 10 min and rinsed five times in sterile water. The sterile seeds were then planted into pots containing a mixture of sterilized 3/1 vermiculite/perlite, respectively. The plants were grown in a greenhouse at 30 °C with a 16 h light/8 h dark cycle. Then, 3 d old seedlings were inoculated with 1 mL of *B. japonicum* suspension per seedling on soil. After 21 d of growth, the nodules with attached root were harvested, plunged into liquid nitrogen, and stored at -80 °C until LAESI analysis.

LAESI-IMS-MS data analysis

Raw mass spectra of root nodules, root segments, and rhizobia cell pellets were processed (MassLynx, 4.1, Waters, Milford, MA) by averaging ten MS scans and performing background subtraction of equal numbers of ESI only scans. A total of three independent biological replicates, each with a technical replicate, were analyzed from each sample group. MetaboAnalyst 3.0, a web-based metabolomic processing software, was used for the univariate, multivariate, and hierarchical clustering analyses. Data normalization was performed by the summing the total spectral intensities for each sample and Pareto scaling was applied, which the square root of the standard deviation was used as the scaling factor. Heat maps were constructed with the Euclidean method for the distance, and the Ward method for the clustering algorithm. PLS-DA provided loadings plots, corresponding to the respective component scores plots

differentiating the classes, which were used to construct the box-and-whisker plots. For univariate analysis, volcano plots were created and only ions that exhibited a $p < 0.05$ based on the Student's t-test and a fold change of > 2 were considered for analysis. Metabolomic pathway coverage was explored using the Soybean Knowledge Base (http;//soykb.org) that allows for multi-omics integration and metabolic pathway analysis tool (Joshi *et al.*, 2014). For pathway topology analysis, a total of 112 significantly high intensity root nodule metabolites were processed using their common compound names and soybean specific KEGG pathways were probed to investigate the metabolite coverage.

Tentative peak assignments were based on a combination of metrics that included first matching the accurate mass results to its potential elemental composition (i.e., possible molecular formula) and searching masses in online databases (Plant Metabolic Network, http://plantcyc.org; and Metlin, https://metlin.scripps.edu). Then by comparing measure tandem MS and CCS values to those in the databases or our internal standards database. Data dependent acquisition was performed for the selection and collision induced dissociation (CID) of parent ions. Collision energies for CID were ramped from 30 to 55 eV. In the IMS experiments, CCS values were calculated based on external calibration by polyalanine with a repeat unit range from n = 4 to n = 14, which spanned the *m/z* range between 233 and 943. To visualize ion intensities as a function of *m/z* and DT, and apply the external calibration to obtain CCS values, the Driftscope software (Waters, Milford,MA) was used. Differences between *m/z* vs. DT plots, the fusion plots, were produced by the HDMS Compare software (Version 1.0, Waters, MA).

SUPPORTING INFORMATION LEGENDS

Figure S1. LAESI-MS analysis of standards, which were selected based on their presence within the intact soybean nodules, illustrates the extent of in-source fragmentation of these metabolites. Adenosine exhibited a 61.4% fragmentation from the observed parent peak to adenine from the LAESI process, as compared to 37.4% in-source fragmentation from ESI alone—therefore, 24.0% of the fragmentation is induced by the laser ablation process. Other compounds showed no parent ion decay (e.g., the glucoside and flavone). The extent of lipid decomposition due to the LAESI-MS technique revealed that in-source fragmentation of lipid species did not yield fatty acid ions, but rather the corresponding ketene cleavage products for the PG and PC species. Furthermore, there was no observed phosphocholine head group from the PC species. (*) Represents unique ions produced during LAESI-MS in-source fragmentation as opposed to ESI alone.

Figure S2. Corresponding negative ion mode data to Figure 3. (A) Heat-map illustrating the major spectral difference based on normalized negative ion spectra, where each column is a spectrum and each row is an *m/z*. The color for the samples of the heat map represents the relative abundance of metabolites: red is greater relative abundance and blue is lower relative abundance. (B) Scores plot from PLS-DA of the spectra, which were used to assist in identifying minor species that are significant in each system with a 95% confidence. The corresponding loadings plots from PLS-DA of the spectra were used to identify peaks of interest. (C) Relative abundances of four significant species as identified from the loadings plots.

Figure S3. Demonstrating the utility of IMS in resolving isobaric species. (A) Box-and-whisker plot of the relative abundance of the *m/z* 203.054 in the root nodule and uninfected root without IMS, where there is no significant difference in the root nodule and uninfected root samples. Implementation of IMS showed two isobaric ions at the nominal mass of *m/z* 203 that were separated based on their unique CCS values. Based on tentative assignments, we see (B) theophylline in more abundant in the nodule and (C) monosaccharide is significantly more present in the uninfected root sample.

Table S1. Relative abundances of the chemical species detected from free-living rhizobia, root nodules, and uninfected root segments with tentative assignments based on the observed *m/z*, tandem MS, collision cross sections, and Metabolomics Standard Initiative (MSI) level of metabolite identification (Sumner et al., 2007).

Experimental procedures S1. *Bradyrhizobium japonicum* USDA110 cell culturing, soybean plant (*Glycine max* Williams 82) growth and bacterial inoculation, followed by plant harvesting and storage. LAESI-IMS-MS data analysis of raw spectra, including statistical analysis procedures. Methods for peaks assignments and metabolic pathway analysis, using IMS and tandem MS data.